Australian Government
Department of Defence
Defence Science and
Technology Group

Topology Model of the Flow around a Submarine Hull Form

S.-K. Lee

Maritime Division
Defence Science and Technology Group

DST-Group–TR–3177

ABSTRACT

A topology model constructed from surface-streamer visualisation describes the flow around a generic conventional submarine hull form at pure yaw angles of 0°, 10° and 18°. The model is used to develop equations for sway-force and yaw-moment coefficients which relate to the hull-form geometry and the flow circulation around the submarine.

Published by

Maritime Division
Defence Science and Technology Group
506 Lorimer St,
Fishermans Bend, Victoria 3207, Australia

Telephone: *1300 333 362*
Facsimile: *(03) 9626 7999*

AR-016-453
December, 2015

APPROVED FOR PUBLIC RELEASE

Topology Model of the Flow around a Submarine Hull Form

Executive Summary

An understanding of the flow around a submarine is necessary to predict the hydrodynamic forces which can affect motion control, safe manoeuvring and signature performance of the submarine.

The focus of this study is on the flow produced by a submarine at yaw angles of 0°, 10° and 18°. Notable flow structures are the counter-rotating longitudinal vortices leeward of the hull and the tip vortex aft of the fin (or sail).

In this report, a topology model of the flow around the submarine has been constructed by using flow-visualisation data obtained from (i) testing with a generic conventional "Joubert" hull form in the Defence Science and Technology Group low-speed wind tunnel at Fishermans Bend, and from (ii) literature review of classical structures known to exist in submarine flows.

The topology model provides an initial step towards developing equations which relate the sway-force and yaw-moment coefficients to the submarine geometry and its surrounding flow. The model equations take into account the slenderness ratio of the hull and the location of the fin, and therefore may be used to compare different generic submarine designs. The equations are calibrated by using circulation, force and moment data from experiments and/or computational-fluid-dynamics (CFD) modelling, and so it is possible to use them for cross-checking measurements and for validating CFD results.

THIS PAGE IS INTENTIONALLY BLANK

Author

Soon-Kong Lee
Maritime Division

S.-K. Lee holds a BEng (Hons), a PhD and a 2009 Doctoral Research Medal from the University of Adelaide. He has worked as a postdoctoral research associate at the University of Newcastle for 3 years before joining the Defence Science and Technology Group in 2013.

THIS PAGE IS INTENTIONALLY BLANK

Contents

Figures

THIS PAGE IS INTENTIONALLY BLANK

Notation

Flow-topology (bifurcation and critical point) symbols

B^+	positive-bifurcation line
B^-	negative-bifurcation line
F	focus/vortex
N	node
S	saddle point

Geometric parameters and body coordinate system

$A_h(x)$	cross-section area of the submarine hull at a given body-axis (x) location
A_p	planform area of the submarine bare hull
c_f	chord length of the fin
h_c	height of the casing measured from the body (x) axis
h_f	height of the fin measured from the casing
L	length of the submarine
$L_{c/4}$	distance from the submarine nose to the quarter-chord point of the (NACA) fin
L_f	distance from the submarine nose to the leading edge of the fin
L_m	distance from the tail plane to the mid-ship (or center of buoyancy) of the submarine
R	slenderness ratio of the submarine bare hull, $R = L/(2r_m)$
r_m	radius of the bare hull at mid-ship (or maximum radius of the bare hull)
x, y, z	body-axis, horizontal and vertical directions

Flow parameters

C_{F_y}	sway-force coefficient
C_{M_z}	yaw-moment coefficient
$\mathrm{F}_{y,f}$	sway force acting on the fin
$\mathrm{F}_{y,h}$	sway force acting on the hull form
$i_{y,h}(x)$	hydrodynamic impulse in the cross-stream (y) direction of the hull form
K_1, K_2	non-dimensionalised moments of vorticity
K_f, K_h	model coefficients for the load on the fin and on the hull form

$M_{z,f,m}$	yaw moment acting on the fin about the mid-ship of the submarine
$M_{z,h,m}$	yaw moment acting on the hull form about the mid-ship of the submarine
Re_L	Reynolds number based on the length of the submarine, $Re_L = LU_\infty/\nu$
U_∞	free-stream velocity
z_c	vertical location of the centroid of a vortex (or region of concentrated vorticity ω_x)

Greek symbols

Γ	circulation
γ_f	model coefficient for vertical location of the fin-tip vortex
γ_h	model coefficient for vertical distance between the counter-rotating hull vortices
κ	dimensionless circulation parameter, $\kappa = \Gamma/[r_m U_\infty \sin(\psi)]$
ν	kinematic viscosity of the working fluid
ω_x	body-axis (x) component of vorticity
ψ	submarine yaw angle
ρ	density of the working fluid

Subscript symbols

a	aft-body (or stern) of the submarine
c	casing (top side)
fb	fin bound vortex (leeward side, for yaw conditions)
fj	fin junction (leading edge)
fl	fin leeward side (for yaw conditions)
fp, fs	fin port and starboard (for straight-ahead and yaw conditions)
ft	fin tip (trailing edge, for yaw conditions)
hb, hc	hull base and casing (leeward side, for yaw conditions)
hl, hw	hull leeward and windward sides (for yaw conditions)
n	nose (or bow) of the submarine

1 Introduction

A submarine performing a yaw manoeuvre can produce some noticeable large-scale flow structures, such as a pair of counter-rotating longitudinal vortices leeward of the hull and a tip vortex aft of the fin. The circulation of these structures are of concern because they can affect the hydrodynamic forces acting on the hull, and hence the motion control and computational-fluid-dynamics (CFD) prediction of safe manoeuvre. Also another major factor is the vibration and noise due to interactions between flow structures and the submarine propulsion, which can affect signature performance.

Low-speed wind-tunnel testing and CFD modelling of submarines by the Defence Science and Technology Group at Fishermans Bend make use of a generic conventional hull form[1] defined by Joubert [1, 2]. The design objectives of this hull form are to provide "minimum practical resistance and minimum water flow noise... while still carrying out all its normal functions" [2]. To reduce resistance and flow noise arising from flow-structure interaction, it is necessary to test the shape of the submarine, which includes the length-to-diameter (i.e. slenderness) ratio of the hull and the location and height of the fin[2]. A key aspect of design testing and CFD validation therefore requires an understanding of the flow structures produced by different parts of the submarine and how they contribute to the hydrodynamic forces during a yaw manoeuvre.

The study presented in this report is twofold: (i) to visualise and establish a detailed topology of flow structures produced by different parts of the submarine (Sections 3-7), and (ii) to develop equations which relate the hydrodynamic forces to the circulation of the flow structures and the shape of the submarine (Sections 8-10).

2 Shape of the Submarine Model

Figure 1 shows the shape of the generic hull form used for this study. The model is developed from a bare hull which has a slenderness ratio of 7.3 to provide minimum resistance [2]. The nose geometry is derived from a NACA-0014.2-N00.20 profile and is axisymmetric for the first 7% of the body length (L) to provide a clean forward sonar. The fin has the shape of a NACA-0015 aerofoil[3] with a rounded trailing edge; the fin height is 8%L, the chord length is 16%L and the leading edge is located at 31%L. The tapering to the end of the tail cone starts at approximately 76%L. The "X"-rudders located at approximately 86-91%L are the aft control surfaces. The present model does not include any hydroplanes.

[1] The term "hull form" used here takes into account the profile of the submarine nose (or bow), the casing and the aft-body (or stern); an axisymmetric hull form with no casing is called a bare hull.

[2] The fin (Commonwealth and European) or the sail (American) refers to the largest appendage on the upper hull of the submarine geometry.

[3] The NACA series is a well-known family of aerofoil shapes developed by the American National Advisory Committee for Aeronautics — NACA has published a wealth of information on aerofoil lift and drag coefficients established from wind-tunnel testing, e.g. [5].

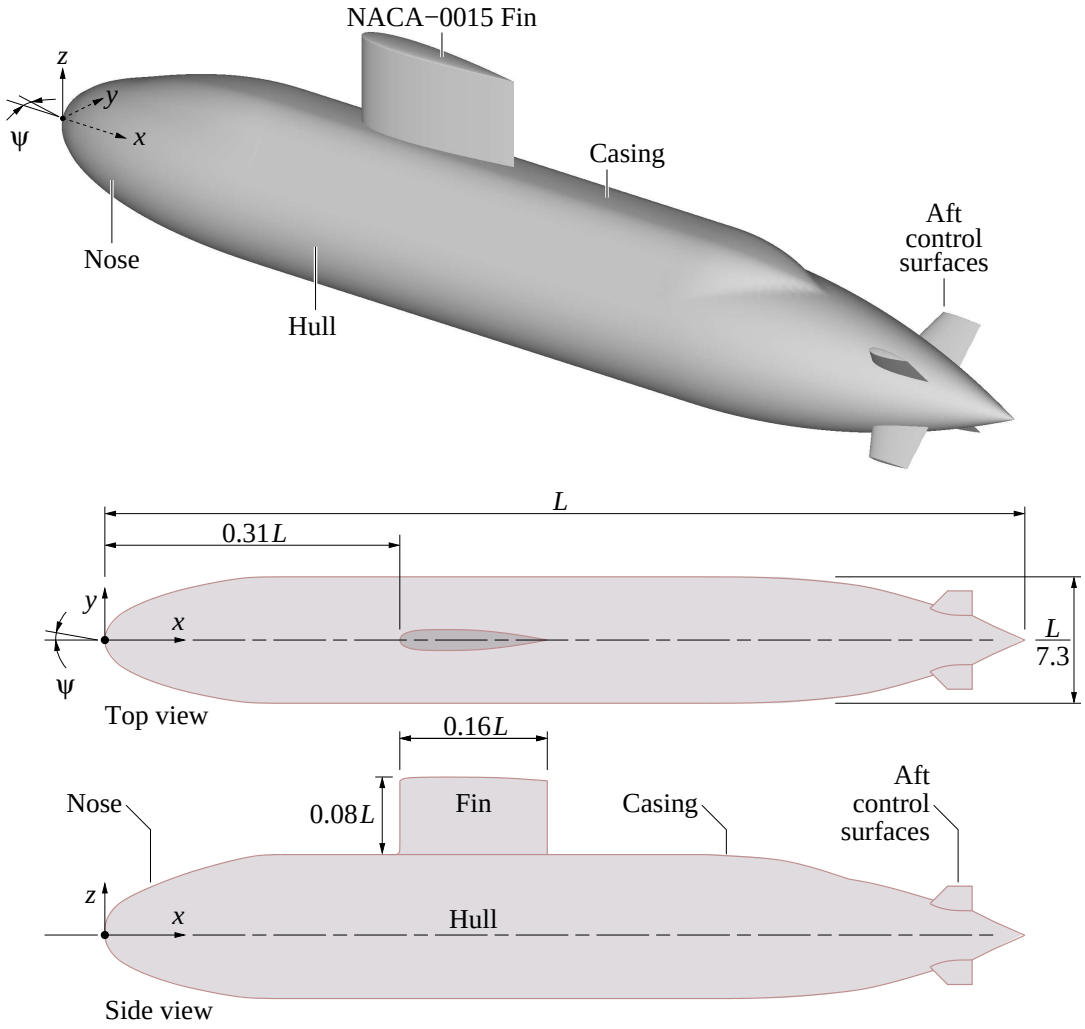

Figure 1: A schematic diagram of the generic conventional hull form defined by Joubert [2].

3 Surface-Streamer Visualisation

Evidence of strong turbulence fluctuation or flow separation is obtained by attaching a series of streamers on the submarine model of length $L = 1.35$ m. The streamers are woollen tufts approximately 10 mm long and 1 mm in diameter. Motion of the streamers in the air flow is observed in the test section (2.7 m wide $\times$ 2.1 m high $\times$ 6.6 m long) of the low-speed wind tunnel at Fishermans Bend [6]. To ensure that the surface shear stress is high enough to make the tufts flutter and that the results are compatible with earlier experiments and simulations [7, 8, 9], the test is performed at a free-stream velocity (U_∞) of 50 m/s. The Reynolds number based on the body length of the submarine is sufficiently large ($Re_L = LU_\infty/\nu = 4.5\times10^6$) such that details of the flow are not sensitive to small changes in the Reynolds number.

To adequately capture details of the surface flow, the streamers are closely distributed on the submarine; to reduce setup time, they are attached only on one side of the body. With the submarine supported on a turntable via two streamlined pylons, it is possible to yaw the body; surface-flow patterns on the windward and leeward sides are obtained by yawing towards starboard and port, respectively. Top-view and side-view images are obtained for three different yaw angles $\psi = 0^\circ$, 10° and 18°. Each image is an ensemble average of 125 frames from a digital video camera (25 frames per second) with the background subtracted to isolate the streamers.

4 Topology of the Submarine Flow

For straight-ahead condition (at zero yaw), the surface-flow pattern is symmetrical about the mirror plane of the submarine (Fig. 2). Inspection of video recording has indicated that the flow pattern is stable, and that there is no visible large-scale separation along the hull. The simplest interpretation in Fig. 3 shows that the surface streaklines begin at a reattachment node (N_n) on the nose and terminate at a separation node (N_a) aft of the submarine. Notable junction-flow features produced by the fin on the casing include a stagnation node-and-saddle (N_{fj} and S_{fj}) pair and a "U-shaped" negative-bifurcation (B_c^-) line. On the casing, a positive-bifurcation (B_c^+) line runs between the legs of the U-shaped negative bifurcation (B_c^-). The enclosed surface-flow pattern (Fig. 3) satisfies the *spherical topology* [3, 4]:

$$\text{number of nodes} - \text{number of saddles} = 2. \tag{1}$$

At 10° yaw, the flow over the submarine is no longer symmetrical (Fig. 4). As the surface of the hull is continuous in the circumferential direction, Fig. 5 shows that the flow spreading from both the windward side (positive bifurcation B_{hw}^+) and the leeward side (positive bifurcation B_{hl}^+) converges on the upper hull (negative bifurcations B_{hc}^- and B_c^-) and on the lower hull (negative bifurcation B_{hb}^-), thus satisfying continuity. On the leeward side of the fin, a streak of fluctuating streamers indicates strong turbulence and separation. In Fig. 5, this feature is shown as a negative-bifurcation (B_{fl}^-) line. Further inspection of video recording have shown possible counter-clockwise rotation of streamers at the leading edge of this bifurcation (B_{fl}^-) line; in the alternate interpretation (Fig. 5), this supplementary feature appears as a surface vortex (focus F_{fl}^*; the existence of saddle S_{fl}^* is deduced from Eq. (1)). Note that the flow in this region is highly turbulent, and that the surface vortex (F_{fl}^*) may be intermittent.

At 18° yaw, the surface flow is different from that obtained at 10° yaw; namely, the flow gradients are steeper along the lines of positive bifurcation (B_{hw}^+ and B_{hl}^+) and there is strong turbulence fluctuation over a larger leeward area of the fin (Fig. 6(a)). From instantaneous images and video recording, clearly observed streamers diverging from a point source on the leeward surface of the fin implies that there is a reattachment node here (Fig. 6(b)). In the interpreted flow field (Fig. 7), strong shear-layer interaction in the vicinity of this reattachment node (N_{fl}) leads to a classical U-shaped separation (negative bifurcation B_{fl}^-) around this node. For the 18°-yaw case to be consistent with the observations for the 10°-yaw case, it is possible to include a supplementary focus-and-saddle (F_{fl}^* and S_{fl}^*) pair in the vicinity of the U-shaped separation, where the topology still satisfies Eq. (1).

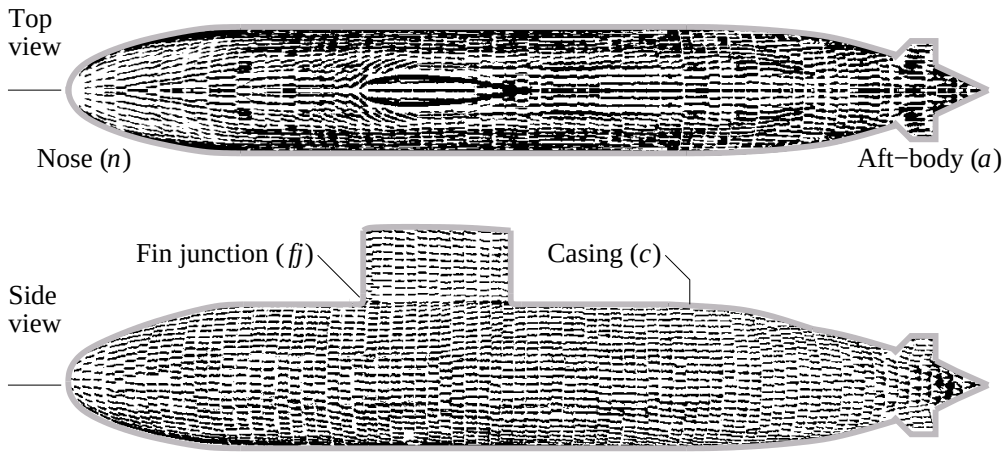

Figure 2: Time-averaged surface-flow pattern on the submarine; $\psi = 0^\circ$. This flow pattern is stable and has the same appearance as the instantaneous surface-flow pattern. The mean flow direction is from left to right.

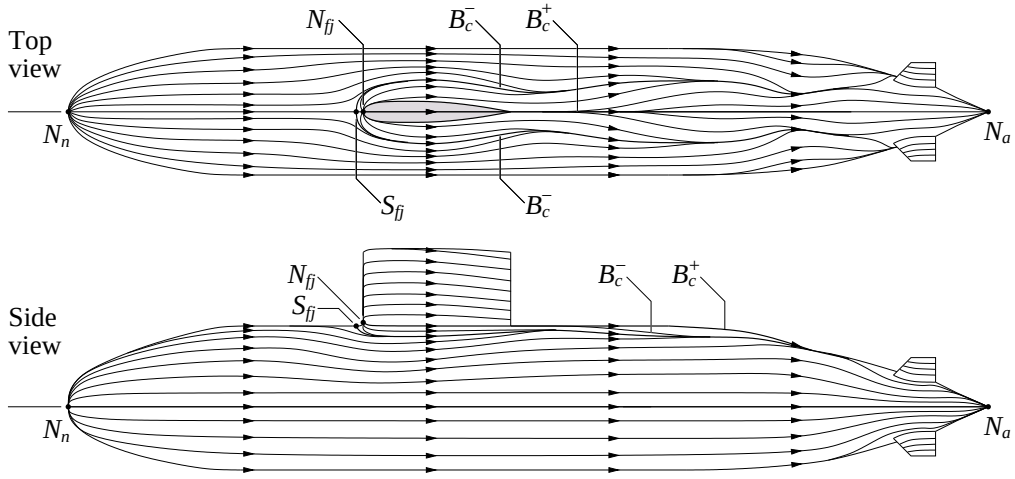

$$N_n + N_a + N_{fj} = \Sigma\text{nodes} = 3$$
$$S_{fj} = \Sigma\text{saddles} = 1$$

Figure 3: Interpretation of Fig. 2 using spherical topology $\Sigma\text{nodes} - \Sigma\text{saddles} = 2$.

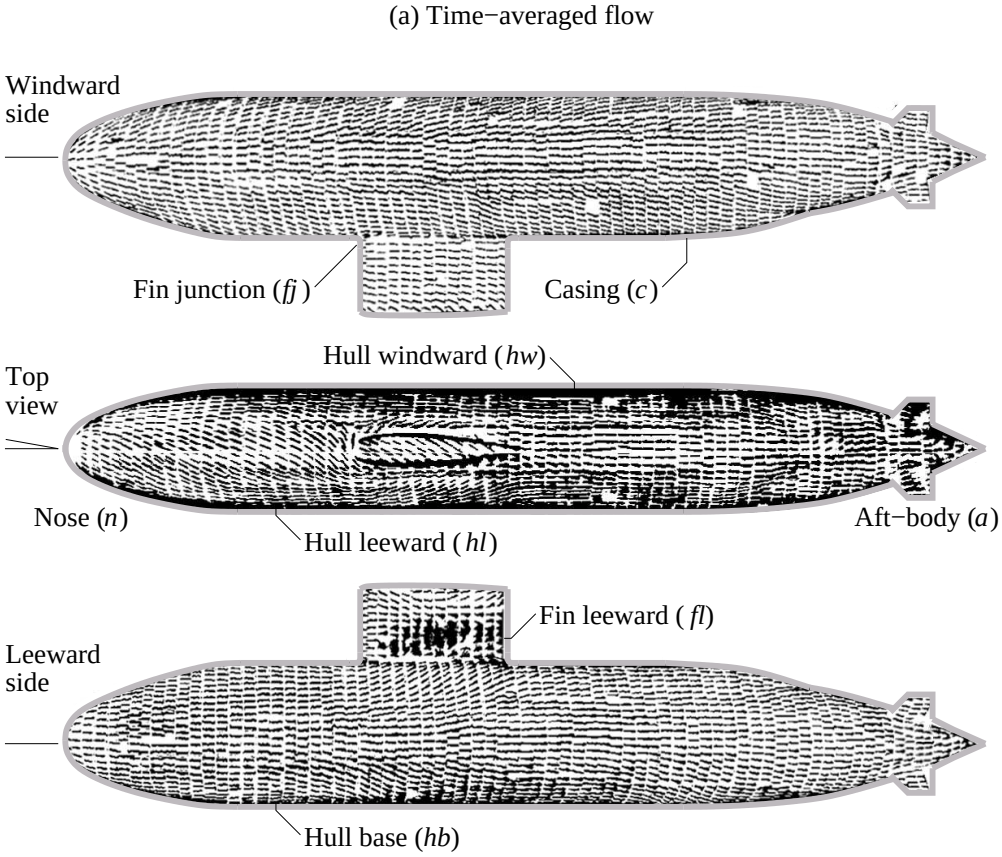

Figure 4: (a) Time-averaged and (b) instantaneous surface-flow pattern on the submarine (in 3rd-angle orthogonal projection); $\psi = 10^\circ$. The mean flow direction is from left to right.

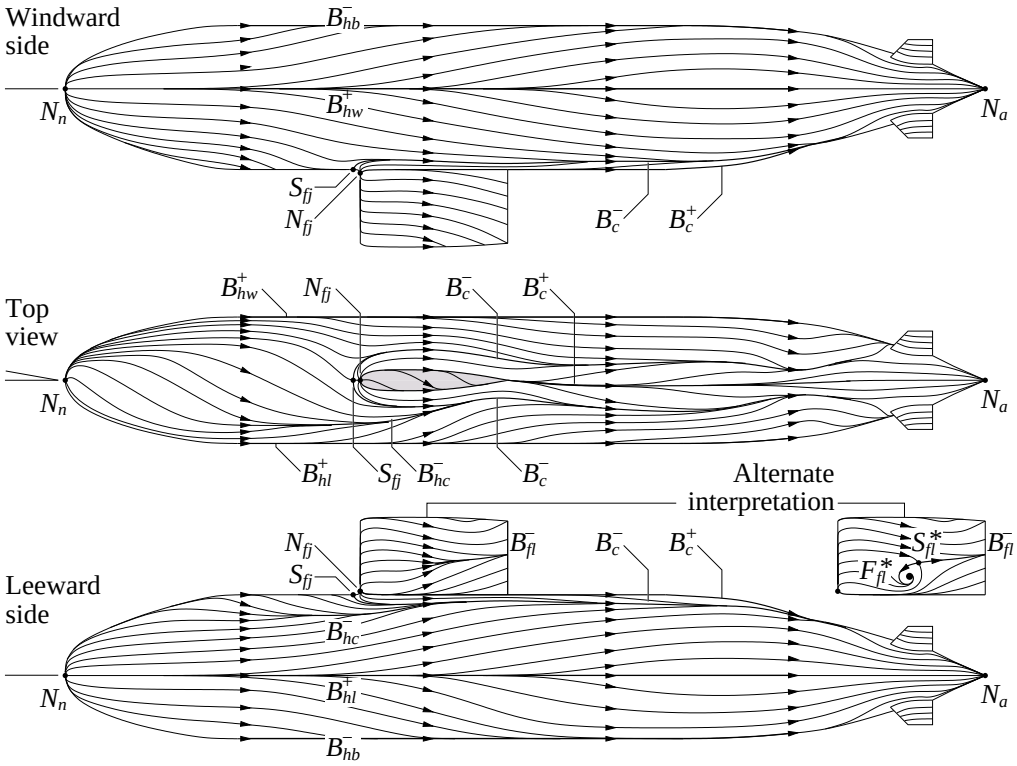

$N_n + N_a + N_{fj} + (F^*_{fl}) = \Sigma\text{nodes} = 4$
$S_{fj} + (S^*_{fl}) = \Sigma\text{saddles} = 2$

Figure 5: Streakline interpretation of Fig. 4 using spherical topology $\Sigma\text{nodes} - \Sigma\text{saddles} = 2$. *In the alternate interpretation, additional critical points are marked with an asterisk (*).*

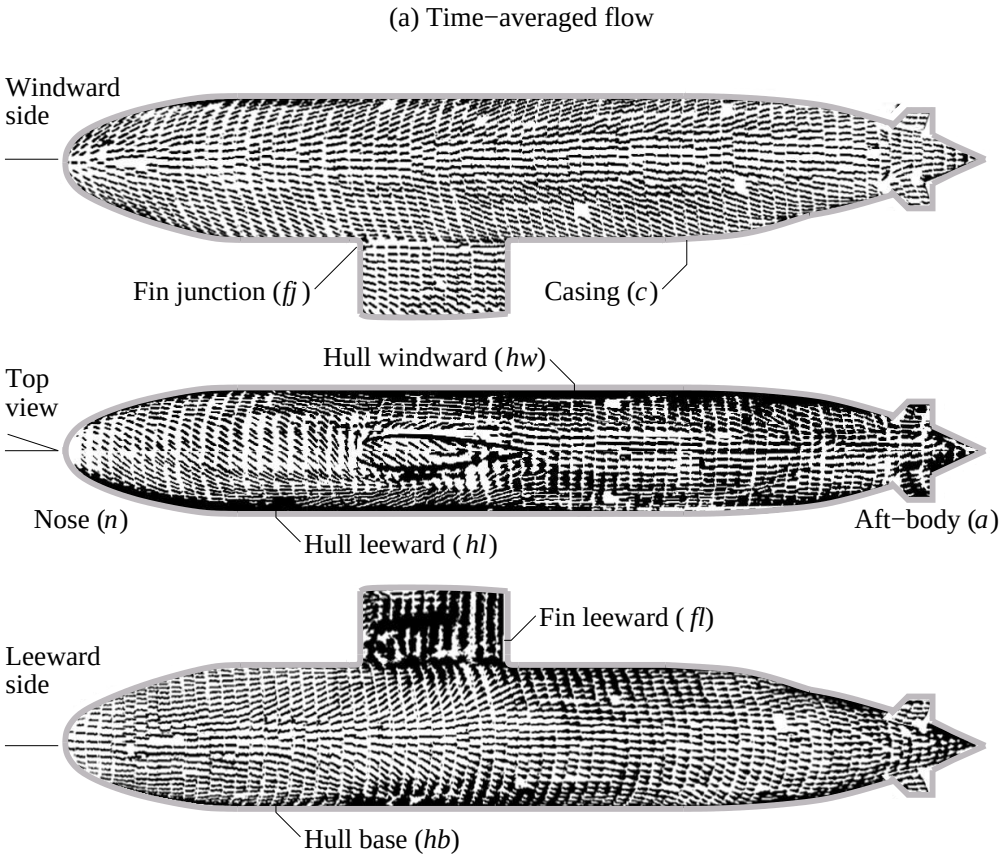

Figure 6: (a) Time-averaged and (b) instantaneous surface-flow pattern on the submarine (in 3rd-angle orthogonal projection); $\psi = 18^\circ$. The mean flow direction is from left to right.

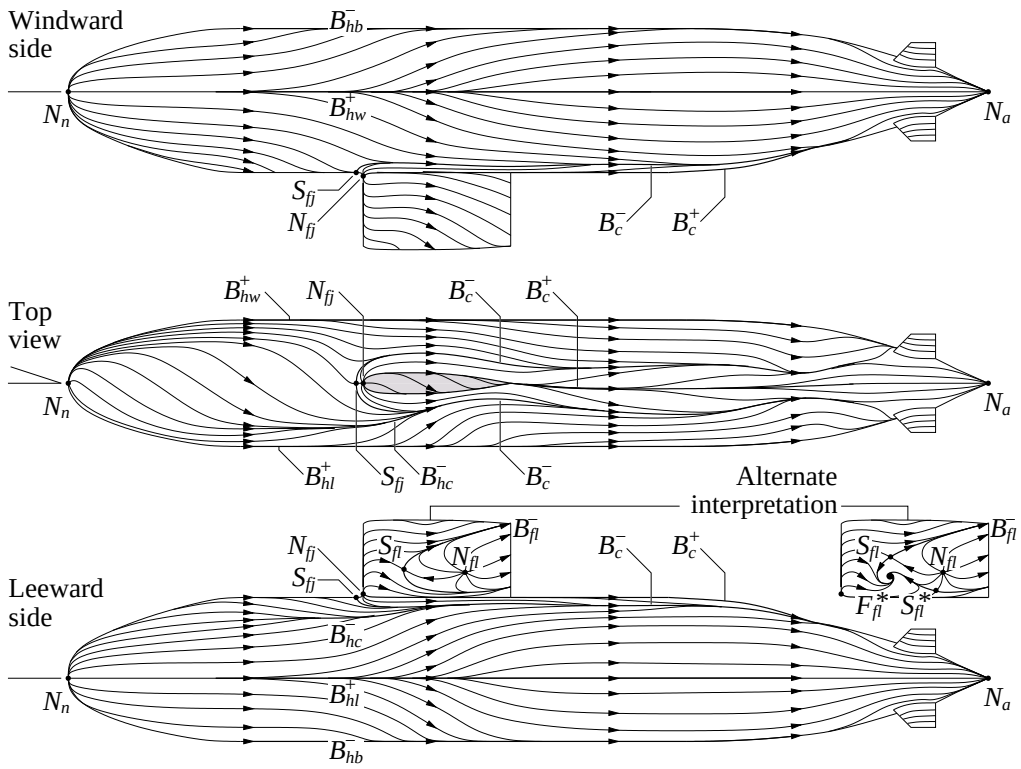

$$N_n + N_a + N_{fj} + N_{fl} + (F^*_{fl}) = \Sigma\text{nodes} = 5$$
$$S_{fj} + S_{fl} + (S^*_{fl}) = \Sigma\text{saddles} = 3$$

Figure 7: Streakline interpretation of Fig. 6 using spherical topology $\Sigma\text{nodes} - \Sigma\text{saddles} = 2$. *In the alternate interpretation, additional critical points are marked with an asterisk (*).*

From three-dimensional reconstruction of the streakline patterns in Figs. 3, 5 and 7, it is possible to infer the main features of the separated flow based on rules of topology [3, 4]. These flow features, as shown in Figs. 8, 9 and 10 for increasing angle of yaw, are identified as follows.

Separation over the nose — As the angle of yaw is increased, the shear layer over the nose separates on the leeward side and rolls up into a pair of counter-rotating eddies (Figs. 8, 9 and 10). Interaction between the shear layer and the hull/casing allows the leeward eddies to grow in size while the local free-stream stretches the eddies into the form of longitudinal vortex legs (F_{hc} and F_{hb}). The leeward vortex legs are on opposite sides of the positive-bifurcation (B^{+}_{hl}) line and they run approximately adjacent to the negative-bifurcation lines along the hull (i.e. vortex leg F_{hc} with line B^{-}_{hc}-B^{-}_{c}; vortex leg F_{hb} with line B^{-}_{hb}). Further details of the flow around the nose are given in Section 5.

Stagnation at the fin junction — On the casing, the turbulent boundary layer separates at the leading edge of the fin and rolls up to form junction eddies. Adverse pressure gradient near the junction leads to the stretching of the eddies into the form of a "horseshoe vortex". In Figs. 8, 9 and 10, the leading edge of the horseshoe vortex (F_{j1}) is located in a recirculation region between the stagnation points (N_{fj} and S_{fj}) at the fin junction. The legs of the horseshoe vortex ($\overline{F_{fp}F_{j1}F_{fs}}$) are on opposite sides of the fin and they run adjacent to the U-shaped negative bifurcation (B^{-}_{c}); increasing the yaw angle increases the asymmetry of the horseshoe vortex. For simplicity, the present topology excludes junction-flow features produced by the control surfaces and supporting pylons; for more details on junction flow, see Section 6.

Formation of the fin-tip vortex — At 0° yaw (Fig. 8), the flow is symmetrical about the mirror plane of the fin and the separation occurs along the tip of the fin to produce a pair of counter-rotating longitudinal eddies. Increasing the angle of yaw reduces the symmetry of the separated flow and redistributes the developing eddies toward the leeward (suction) side.

At 10° yaw (Fig. 9), an asymmetrical flow is established and the separation along the tip of the fin is accompanied by a strong negative bifurcation (B^{-}_{fl}) on the leeward face of the fin. With a sufficiently high shear stress, this bifurcation (B^{-}_{fl}) line can terminate as a focus (F^{*}_{fl}). In Fig. 9, this focus (F^{*}_{fl}) is the end of a line vortex which rises from the surface of the fin and, because the line vortex is embedded in the wake of the fin, it is drawn downstream of the fin as a longitudinal vortex. Since the vortex legs from the surface focus (F^{*}_{fl}) and from the tip of the fin have the same rotation sense, both legs combine to form the fin-tip vortex (F_{ft}).

By increasing the yaw angle from 10° to 18°, the leeward flow further produces a reattachment node (N_{fl}) on the fin. In Fig. 10, the shear layer separating around this node (N_{fl}) rolls up into a U-shaped vortex. Near the base of the fin, the U-shaped vortex leg combines with the horseshoe leg from the junction vortex (F_{j1}) of the same rotation sense (clockwise F_{fp}); near the top of the fin, the U-shaped vortex leg combines with the fin-tip vortex of the same rotation sense (counter-clockwise F_{ft}). The portion of the U-shaped vortex in the spanwise direction of the fin is known as the "bound vortex".

As shown in Figs. 9 and 10 for the 10°-yaw and 18°-yaw cases respectively, the exclusion or inclusion of the surface vortex (F^{*}_{fl}) on the fin produces only minor changes to the overall flow topology. Further description of the fin-tip vortex is provided in Section 7.

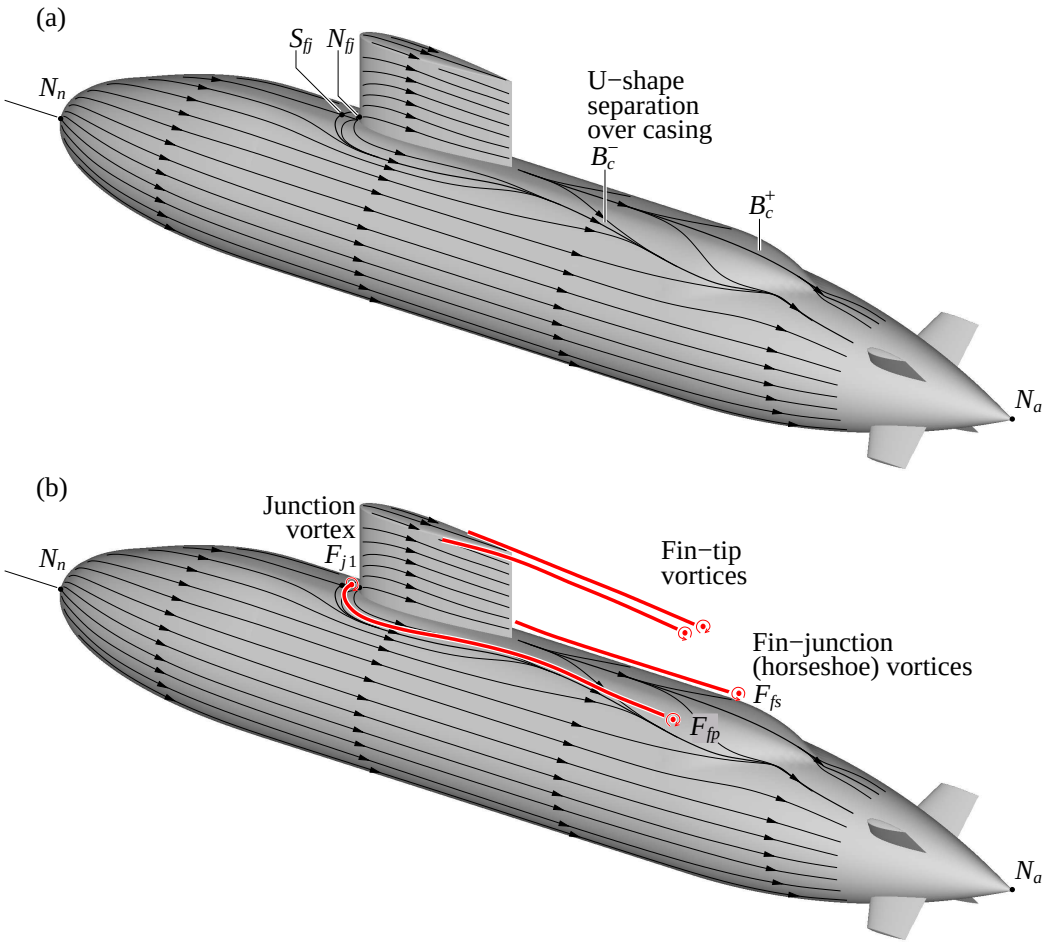

Figure 8: Three-dimensional representation of the flow field; $\psi = 0^\circ$. (a) Time-averaged surface streaklines and (b) vortex lines. The mean flow direction is from left to right.

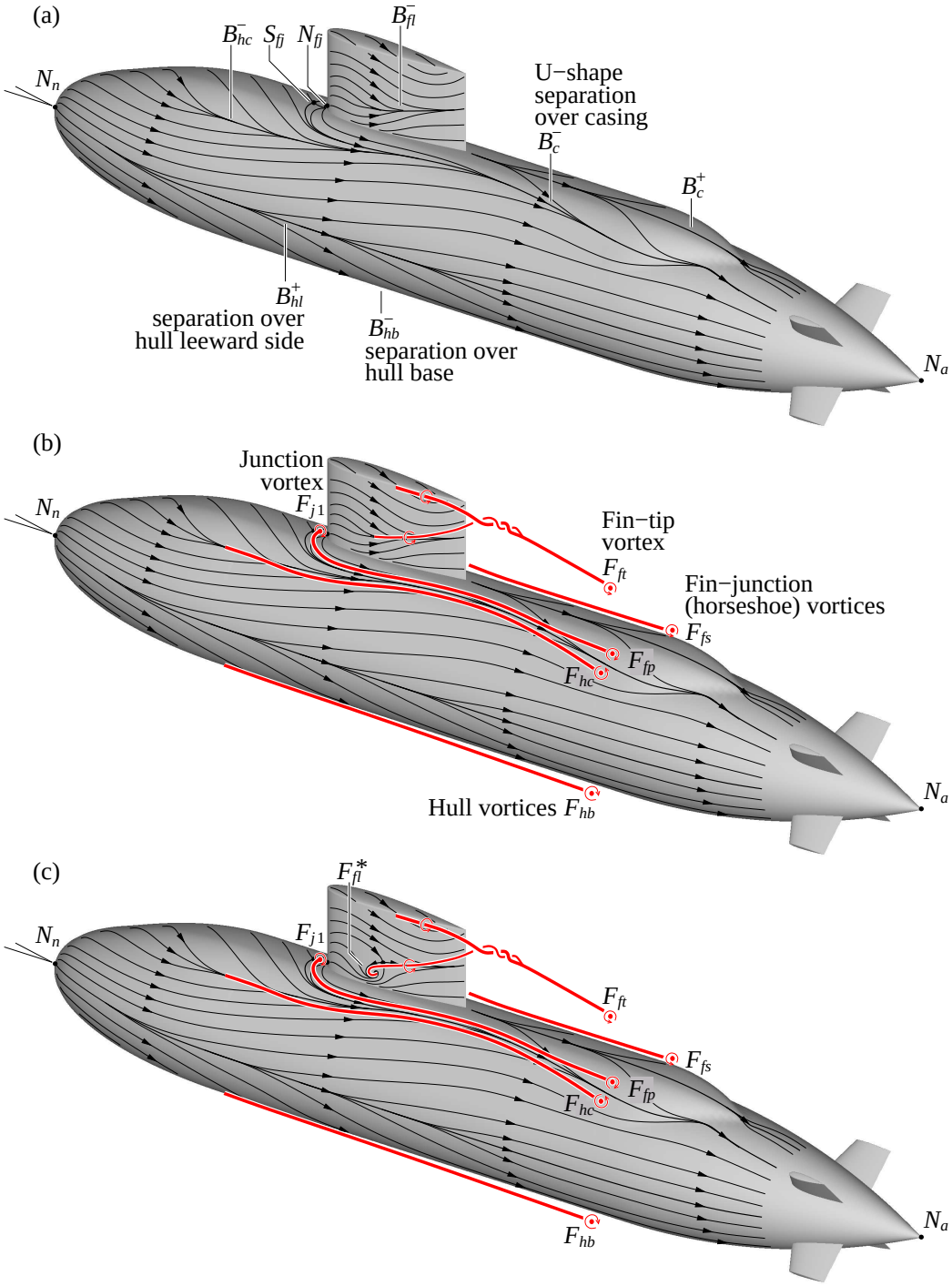

Figure 9: Three-dimensional representation of the leeward flow field; $\psi = 10^\circ$. (a) Time-averaged surface streaklines, (b) vortex lines and (c) alternate interpretation with surface vortex (F_{fl}^*) on the fin. The mean flow direction is from left to right.

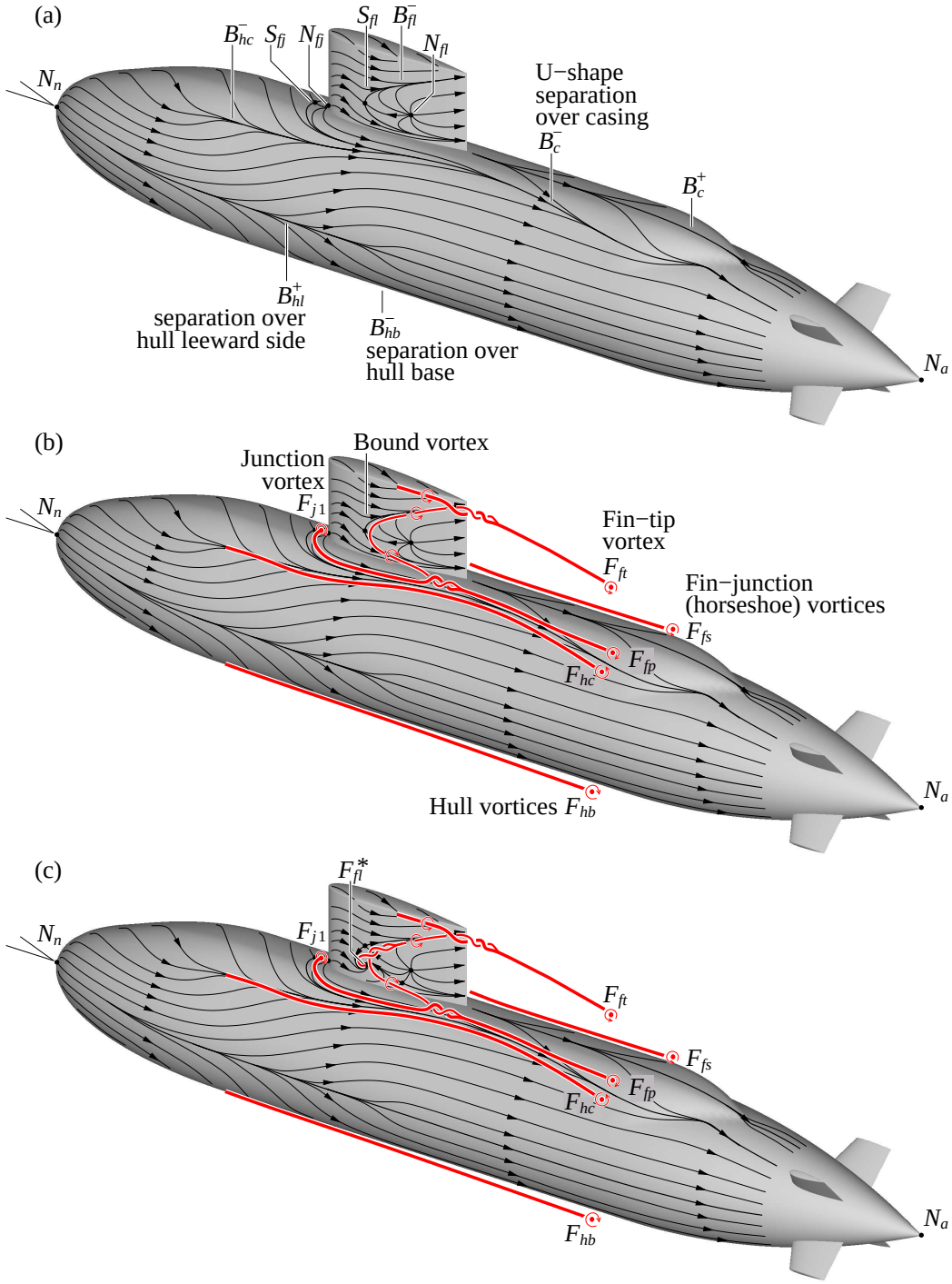

Figure 10: Three-dimensional representation of the leeward flow field; $\psi = 18°$. (a) Time-averaged surface streaklines, (b) vortex lines and (c) alternate interpretation with surface vortex (F^*_{fl}) on the fin. The mean flow direction is from left to right.

5 Flow around the Nose

Figure 11 shows the effect of increasing yaw angle on the surface streaklines and the cross-stream around the nose; three-dimensional representation of the flow is given in Fig. 12. The sequence of flow is inferred from present laboratory observations, previous work on similar (*ellipsoidal*) nose forms [4] and from standard topology rules.

For zero and very small angles of yaw ($0 \leq \psi < 5^\circ$), Figs. 11(a) and 12(a) show that the flow is everywhere attached to the nose and that surface streaklines originate from the tip of the nose at the node N_n. With a minor asymmetry in circumferential pressure, streaklines tend to diverge on the windward side to produce a weak positive bifurcation (B^+_{hw}). On the leeward side, the flow pressure is lower and the converging streaklines form a weak negative bifurcation (B^-_{hl}). In cross-section of the surface flow, the positive bifurcation (B^+_{hw}) is a "reattachment" half-saddle (S_{hw}) and the negative bifurcation (B^-_{hl}) is a "separation" half-saddle (S'_{hl}). The interpreted flow on a two-dimensional plane cutting the submarine body satisfies the *cross-sectional topology* [3, 4]:

$$\text{number of nodes} - \text{number of saddles} = -1. \tag{2}$$

As the yaw angle is increased ($5^\circ \lesssim \psi < 10^\circ$), the flow over the nose becomes locally unstable and this produces an array of dissipative structures. On the surface of the nose shown in Figs. 11(b) and 12(b), they appear as an array of very fine alternating local positive- and negative-bifurcation lines. These structures scale with the thickness of the boundary layer and they resemble an array of eddies moving approximately in the direction of the local mean flow. Since the structures are very small, they have negligible effect on the global flow pattern; however, the inclusion of these (x-number of) eddies has to preserve topology (Eq. (2); Fig. 11(b)).

For larger yaw angles ($10^\circ \lesssim \psi < 20^\circ$), the flow near the tip of the nose becomes less stable and this leads to the formation of new structures similar to those developed further downstream at smaller angles of yaw. Downstream of the nose, the older (eddy) structures coalesce to produce larger local (vortex) structures. Eventually, the effect of these larger local structures becomes significant enough to redistribute the surface shear stress and alter the flow pattern in the vicinity of the nose. In cross-section of the altered surface-flow pattern (Fig. 11(c)), the "reattachment" half-saddle (S_{hl}) corresponds to a positive bifurcation (B^+_{hl}) and the "separation" half-saddles (S_{hc} and S_{hb}) correspond to respective lines of negative bifurcation (B^-_{hc} and B^-_{hb}). In Fig. 12(c), the flow separating from the lines of negative bifurcation (B^-_{hc} and B^-_{hb}) rolls up to produce a pair of counter-rotating longitudinal vortices (F_{hc} and F_{hb}). From visualisation experiments, these vortices have been identified by helical twisting of dye (or smoke) filaments in the separated flow [10], as shown by the example in Fig. 13.

With further increase in the angle of yaw ($\psi \gtrsim 20^\circ$), the redistributed shear stress is sufficient to produce a pair of counter-rotating surface foci (F^*_{hc} and F^*_{hb}) at the leading edge of the negative-bifurcation (B^-_{hc} and B^-_{hb}) lines. In Figs. 11(d) and 12(d), the vortex core rising from each focus is stretched downstream of the nose to form a vortex pair ($\overline{F^*_{hc}F_{hc}}$ and $\overline{F^*_{hb}F_{hb}}$), known as the Werlé-Legendre horn vortices. Figure 14(a) shows a classical side-view profile of a horn vortex obtained from dye visualisation [4]. In Fig. 14(b, c), the surface-flow pattern produced on the leeward side of the nose/hull is topologically the same as those shown in Figs. 11(d) and 12(d).

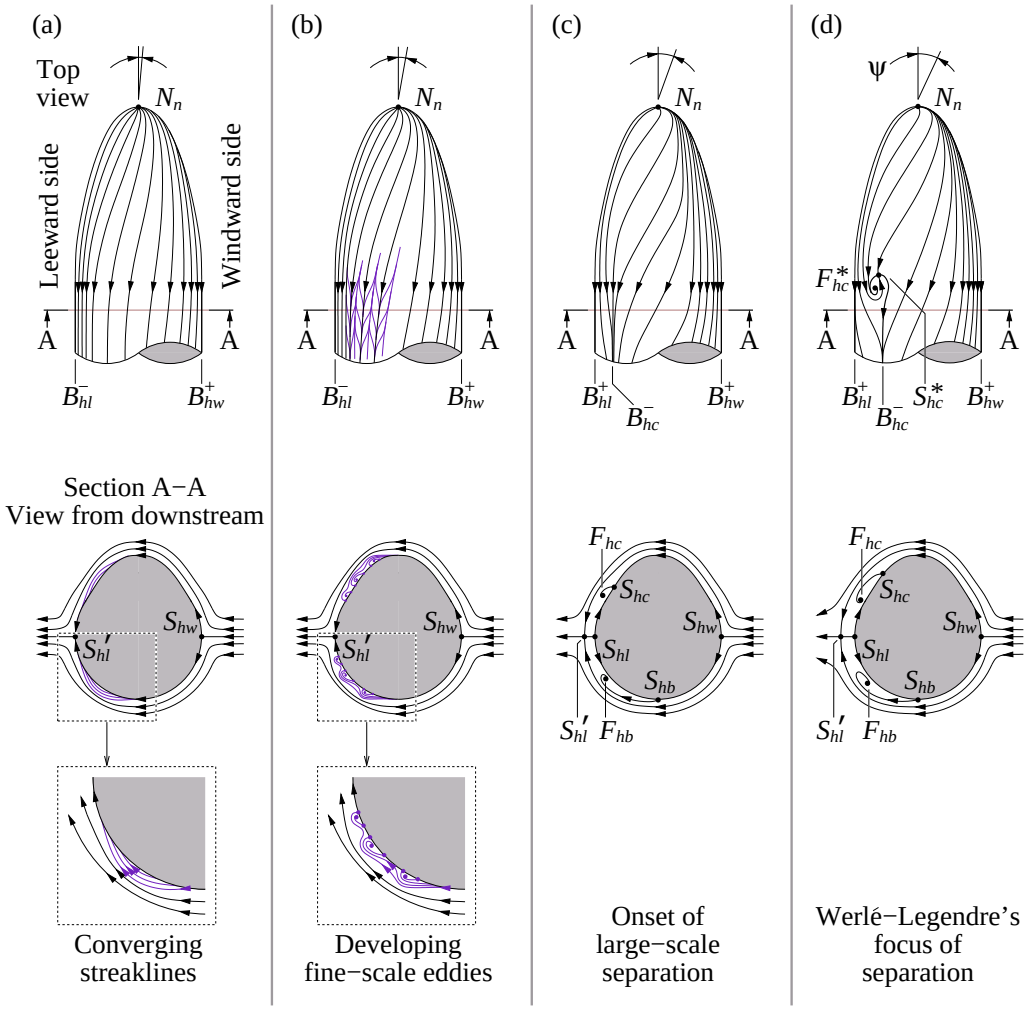

(a)	$\Sigma\text{nodes} = 0$
	$\frac{1}{2}S_{hw} + \frac{1}{2}S'_{hl} = \Sigma\text{saddles} = 1$
(b)	$x(F_{\text{eddies}}) = \Sigma\text{nodes} = x$
	$\frac{1}{2}S_{hw} + \frac{1}{2}S'_{hl} + 2x(\frac{1}{2}S_{\text{eddies}}) = \Sigma\text{saddles} = 1 + x$
(c, d)	$F_{hc} + F_{hb} = \Sigma\text{nodes} = 2$
	$\frac{1}{2}S_{hw} + \frac{1}{2}S_{hl} + S'_{hl} + \frac{1}{2}S_{hc} + \frac{1}{2}S_{hb} = \Sigma\text{saddles} = 3$

Figure 11: Streaklines on the submarine nose (top view, the mean flow direction is downwards) showing the effect of increasing yaw angle, after [4]. In cross-section (A-A), the flow is viewed from the downstream end of the hull, with cross-sectional topology $\Sigma\text{nodes} - \Sigma\text{saddles} = -1$. *For a three-dimensional representation of each surface flow, see Fig. 12.*

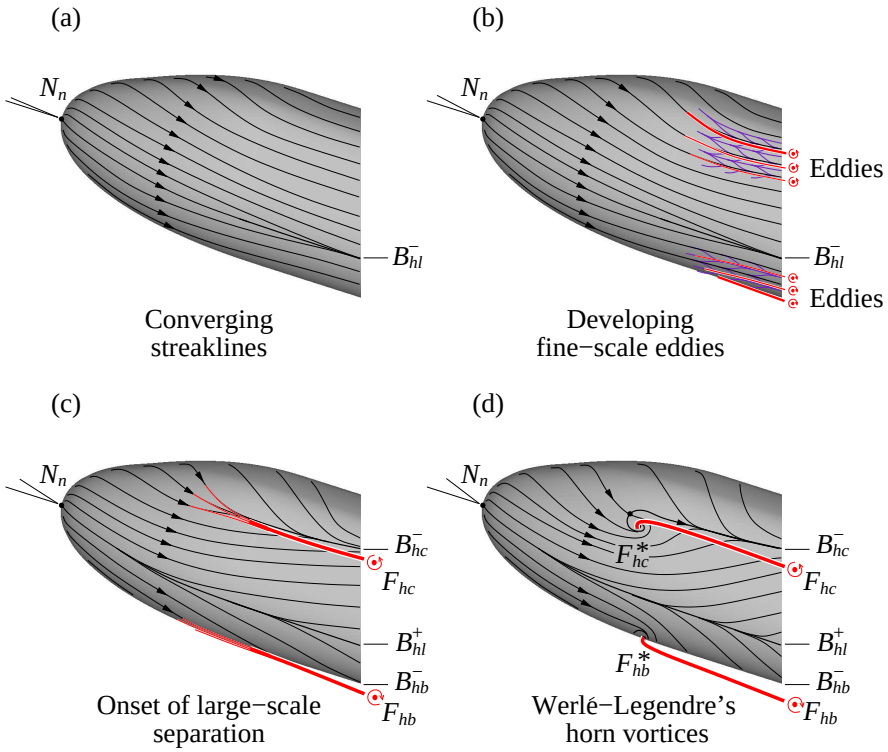

Figure 12: Vortex lines on the leeward side of the nose showing the effect of increasing angle of yaw. For evidence of the nose/hull vortices and the Werlé-Legendre focus of separation, see Figs. 13 and 14, respectively. The mean flow direction is from left to right.

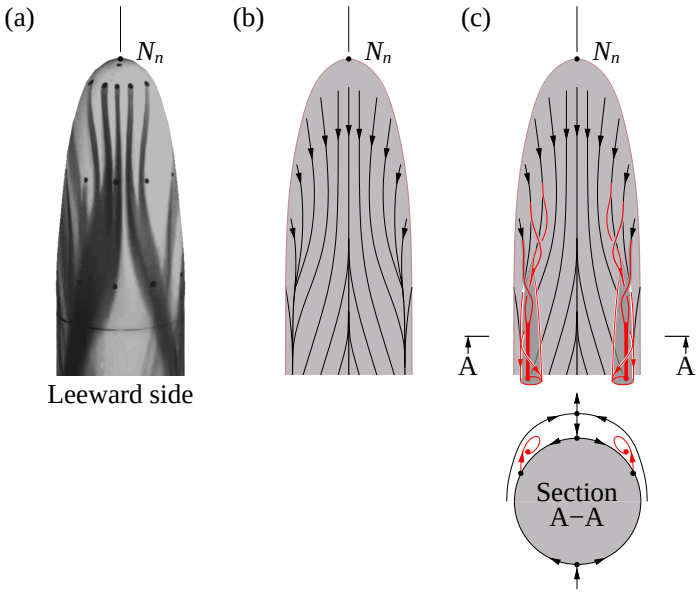

Figure 13: Flow visualisation of the nose/hull vortices for $\psi = 15°$; (a) dye filaments in water [10] and the interpretation of (b) surface streaklines and (c) vortex lines. From side view, the mean flow direction is downwards. In cross-section (A-A), the flow is viewed from downstream of the nose.

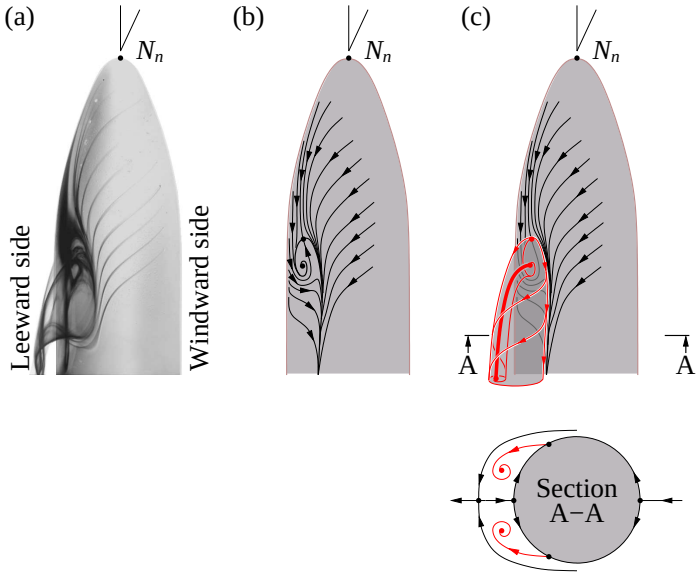

Figure 14: Flow visualisation of the Werlé-Legendre focus of separation for $\psi \gtrsim 20°$; (a) dye filaments in water [4] and the interpretation of (b) surface streaklines and (c) vortex lines. From side view, the mean flow direction is downwards. In cross-section (A-A), the flow is viewed from downstream of the nose.

6 Junction Flow at the Root of the Fin

Figure 15 shows an enlarged view of the junction flow at the fin. In the vertical symmetry plane of the fin, the surface node N_{fj} and saddle S_{fj} are projected as half saddles S'_{j1} and S_{j1}, respectively. In the flow approaching the fin junction, the boundary layer separates and develops a series of horseshoe vortices under a streamwise pressure gradient; these horseshoe vortices are subsequently stretched around the fin under a spanwise pressure gradient. During vortex stretching, new vortices are formed upstream of the oldest horseshoe vortex; topology study (e.g. [11]) has shown that it is possible to have up to three primary horseshoe vortices in junction flows. In Fig. 15, the primary vortices (F_{j1}, F_{j2} and F_{j3}) have the same rotation sense as does the vorticity of the approaching boundary flow; the accompanying eddies (F_{e1}, F_{e2} and F_{e3}) are in the opposite rotation sense to satisfy the *regional topology* [3, 4]:

$$\text{number of nodes} - \text{number of saddles} = 0. \tag{3}$$

At large Reynolds numbers, the primary vortices can induce velocity components on themselves and on the accompanying eddies, and this can lead to (i) the stretching or diffusion of vorticity, (ii) the "leapfrogging" of vortices between one another, and (iii) the merging of vortices to form a larger vortex [11]. Over time, the largest/oldest vortex (closest to the fin) breaks down (due to vortex stretching) while the newer vortices grow and subsequently combine with the remains of the oldest vortex; this process is repeated but is generally aperiodic [11].

Figure 16 shows a classical time-averaged surface-oil flow pattern around a NACA fin which resembles topologically the streamer pattern obtained from the present geometry (Section 4). Moreover, the oil-visualisation pattern in Fig. 16 has been obtained from a much larger fin geometry (30.5 cm chord $\times$ 22.9 cm span) [12], which makes it possible to observe the finer details of the surface flow — for example, the line of low mean shear between the primary stagnation point and the fin.

In the enlarged view provided in Fig. 17, the regions of low mean shear stress and/or stagnation are indicated by areas with high deposit of oil (or large patches of white). From Fig. 17, it is possible to describe the primary horseshoe vortices in relation to the surface-flow pattern upstream of the fin. The interpreted streaklines in Fig. 18 show the primary stagnation as a saddle point (S_{fj}); the surface flow separating from this saddle point (S_{fj}) is visible as a U-shaped negative bifurcation (B_c^-). Time-averaged reverse flow between the saddle point (S_{fj}) and the fin is evidence of recirculation produced by the first horseshoe vortex (F_{j1}); accompanying this vortex is the corner eddy (F_{e1}) which runs along the root of the fin.

In Fig. 19, the line of low mean shear is indicated by the shaded region between the half saddles (S_{e2} and S'_{e2}) and is topologically consistent with the recirculation eddy (F_{e2}) which accompanies the second horseshoe vortex (F_{j2}). As shown in the surface-oil flow pattern (Fig. 16), this line of low mean shear merges with the line of negative bifurcation (B_c^-) to form the legs of the U-shaped separation.

Figure 20 shows that, in comparison with the first and second vortices (F_{j1} and F_{j2}), the third vortex (F_{j3}) and its accompanying eddy (F_{e3}) are much smaller, and given their close proximity to the primary stagnation point (S_{fj}) they are largely embedded in the leading-edge separation (B_c^-). Since all three vortices (F_{j1}, F_{j2} and F_{j3}) have the same rotation sense, the legs on each side of these horseshoe vortices eventually merge with one another by their induced velocity; the combined vortex legs run adjacent to the U-shaped negative bifurcation (B_c^-).

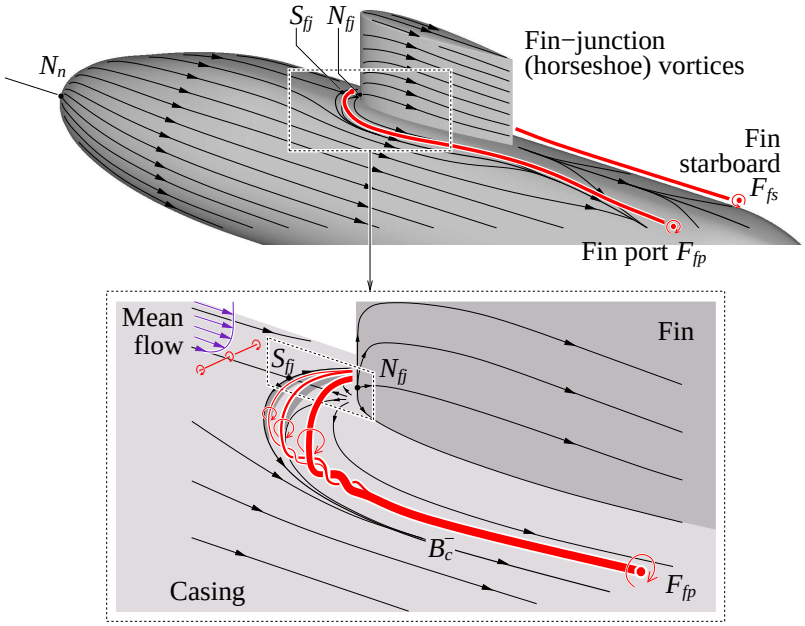

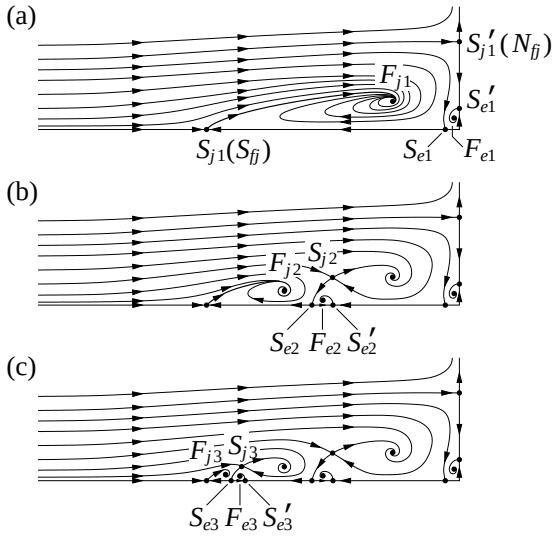

(a)	$F_{j1} + F_{e1} = \Sigma\text{nodes} = 2$
	$\frac{1}{2}S_{j1} + \frac{1}{2}S'_{j1} + \frac{1}{2}S_{e1} + \frac{1}{2}S'_{e1} = \Sigma\text{saddles} = 2$
(b)	$F_{j1} + F_{e1} + F_{j2} + F_{e2} = \Sigma\text{nodes} = 4$
	$\frac{1}{2}S_{j1} + \frac{1}{2}S'_{j1} + \frac{1}{2}S_{e1} + \frac{1}{2}S'_{e1} + S_{j2} + \frac{1}{2}S_{e2} + \frac{1}{2}S'_{e2} = \Sigma\text{saddles} = 4$
(c)	$F_{j1} + F_{e1} + F_{j2} + F_{e2} + F_{j3} + F_{e3} = \Sigma\text{nodes} = 6$
	$\frac{1}{2}S_{j1} + \frac{1}{2}S'_{j1} + \frac{1}{2}S_{e1} + \frac{1}{2}S'_{e1} + S_{j2} + \frac{1}{2}S_{e2} + \frac{1}{2}S'_{e2} + S_{j3} + \frac{1}{2}S_{e3} + \frac{1}{2}S'_{e3} = \Sigma\text{saddles} = 6$

Figure 15: Junction flow at the leading edge of the fin with side-view regional topology $\Sigma\text{nodes} - \Sigma\text{saddles} = 0$*, after [11]. The mean flow direction is from left to right.*

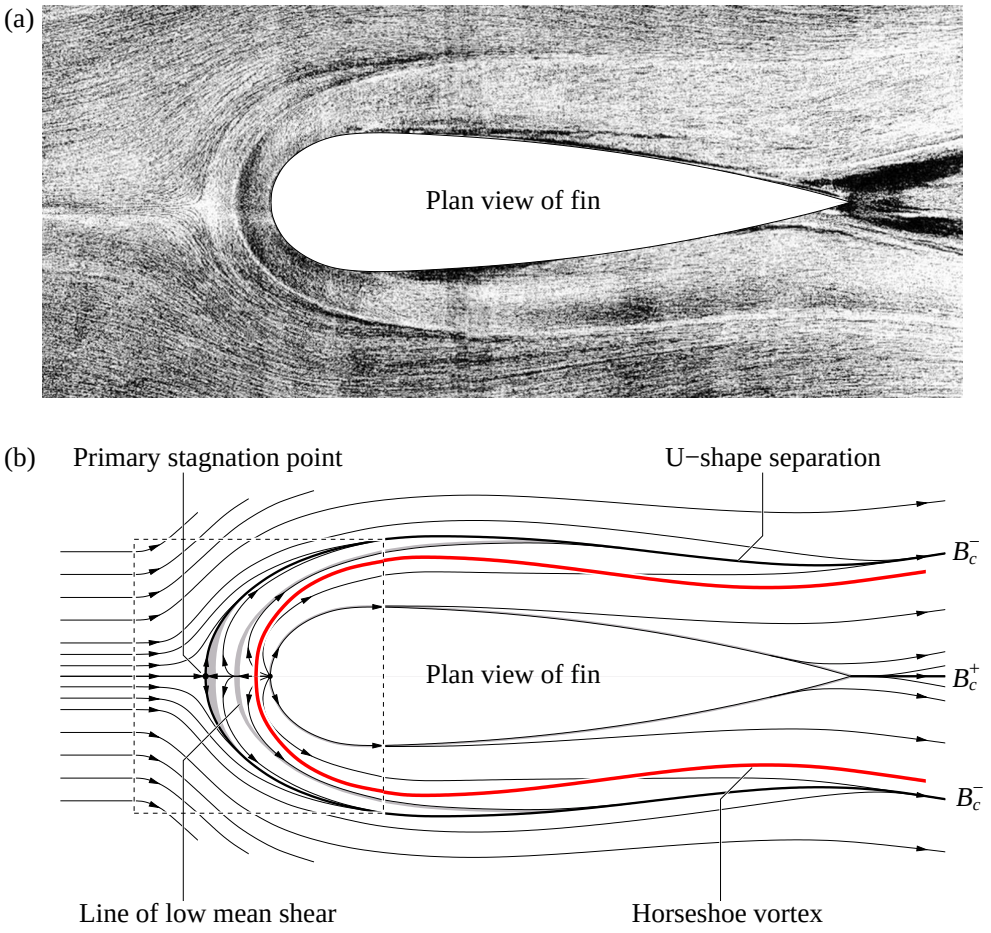

Figure 16: (a) Time-averaged surface-oil flow pattern around a NACA fin [11]. (b) Streakline interpretation. The mean flow direction is from left to right. For details of the flow shown in the dashed box, see Figs. 17-20.

Figure 17: An enlarged view of Fig. 16 showing the time-averaged surface-oil flow pattern at the junction of a NACA fin [11].

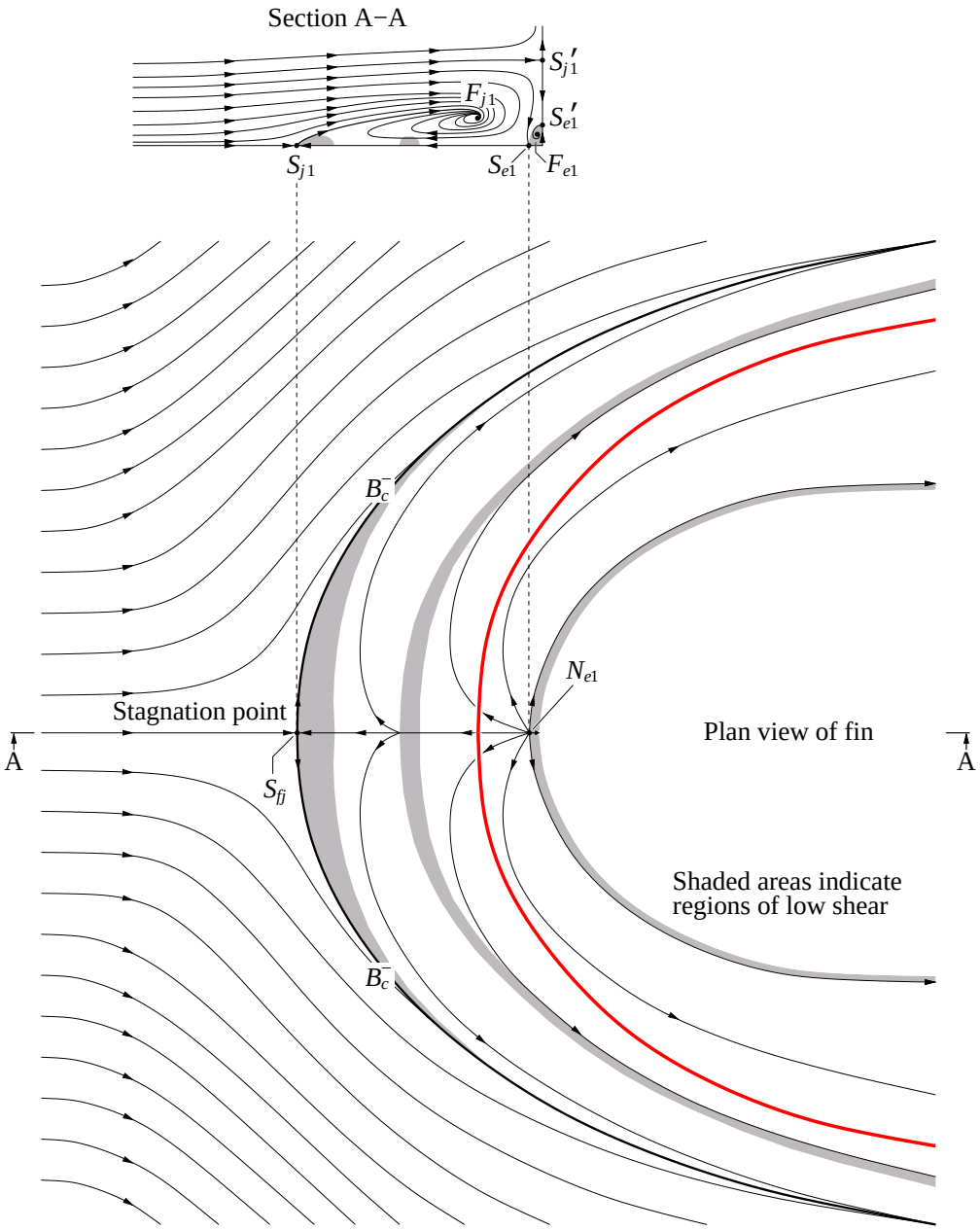

Section A-A	See Fig. 15(a) for details
Plan view	N_{e1} = Σnodes = 1
	S_{fj} = Σsaddles = 1

Figure 18: Streakline interpretation of Fig. 17 showing plan-view regional topology $\Sigma\text{nodes} - \Sigma\text{saddles} = 0$ *with one horseshoe vortex.*

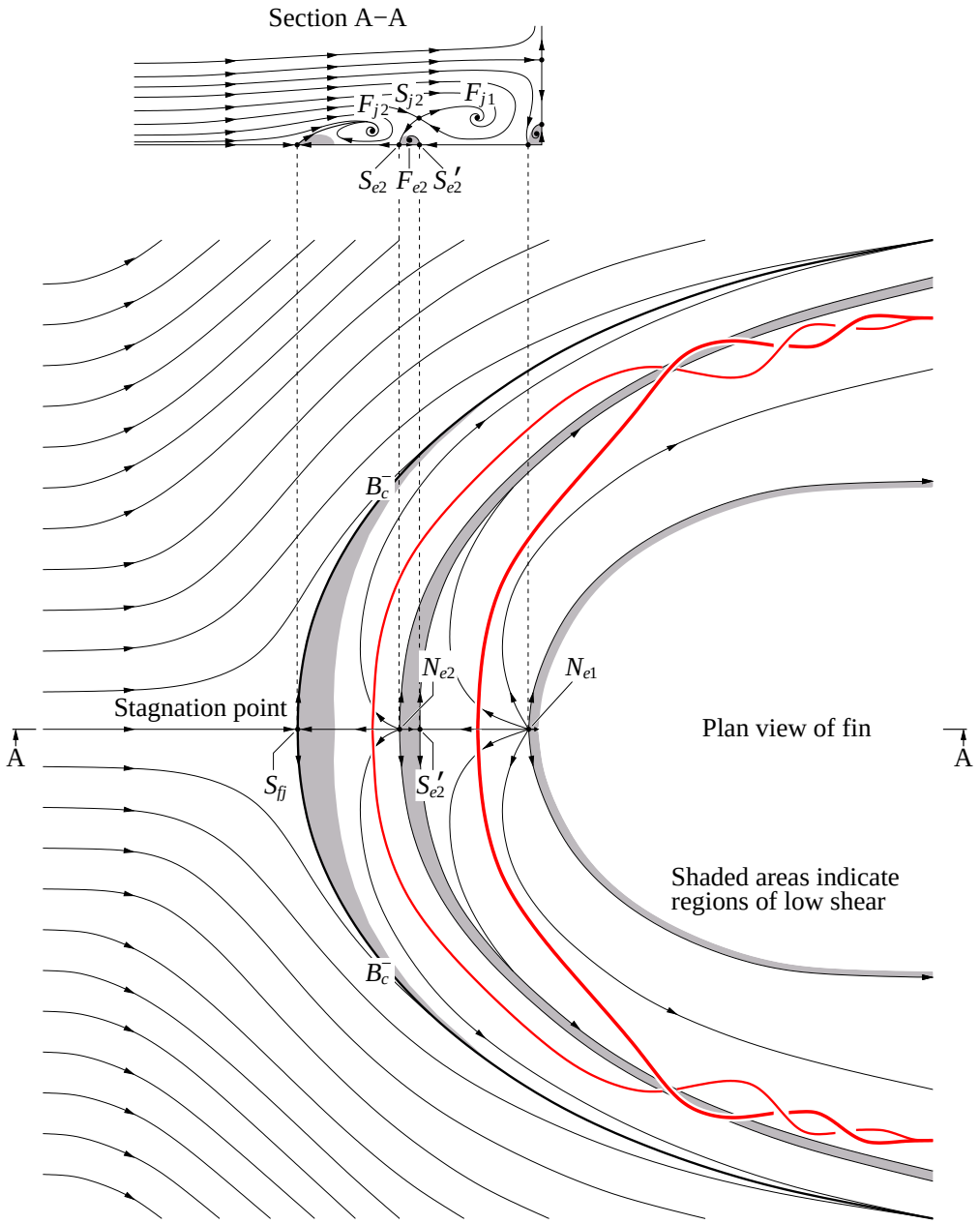

Section A-A	See Fig. 15(b) for details
Plan view	$N_{e1} + N_{e2} = \Sigma\text{nodes} = 2$
	$S_{fj} + S'_{e2} = \Sigma\text{saddles} = 2$

Figure 19: Streakline interpretation of Fig. 17 showing plan-view regional topology $\Sigma\text{nodes} - \Sigma\text{saddles} = 0$ *with two horseshoe vortices.*

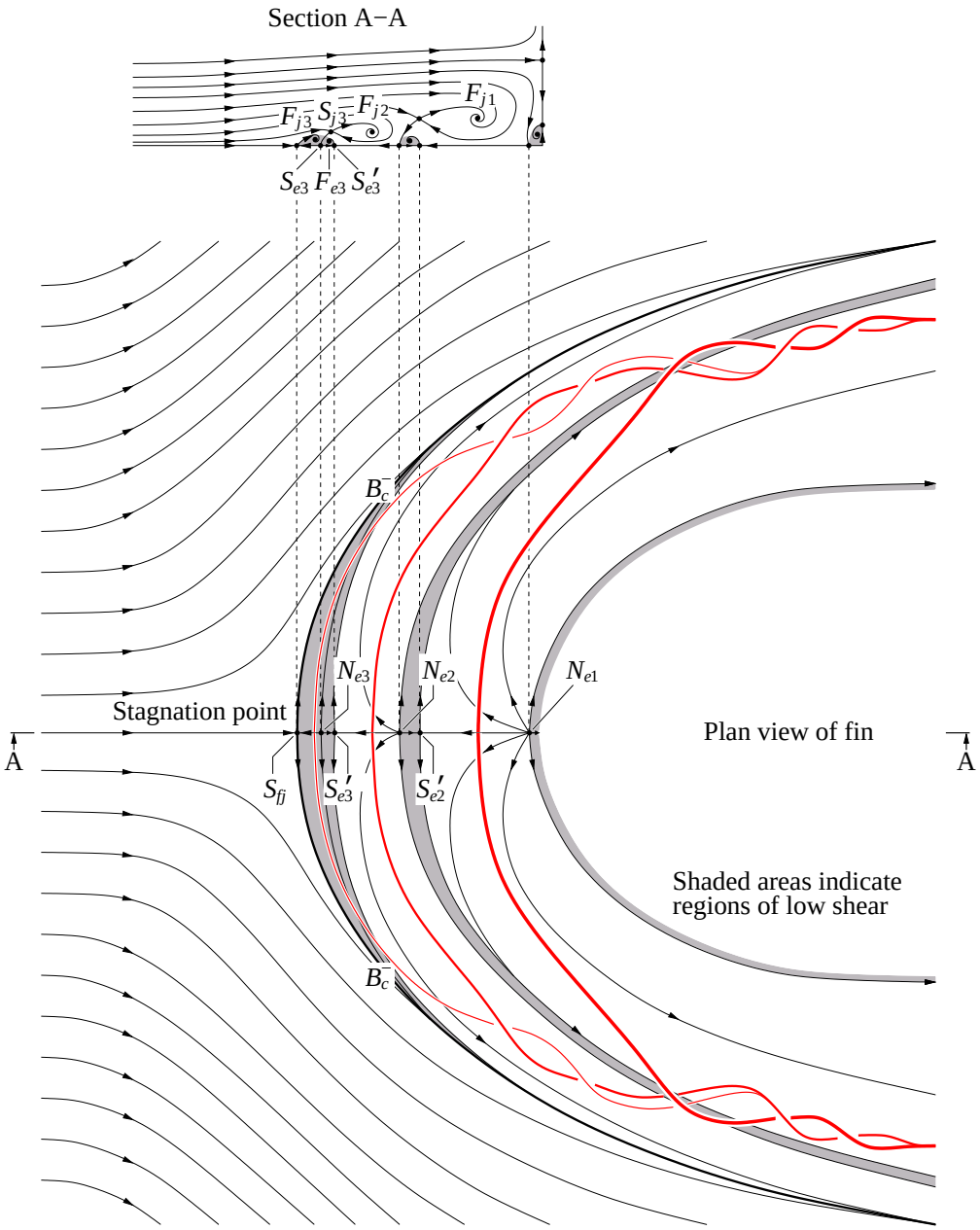

Section A-A	See Fig. 15(c) for details
Plan view	$N_{e1} + N_{e2} + N_{e3} = \Sigma\text{nodes} = 3$
	$S_{fj} + S'_{e2} + S'_{e3} = \Sigma\text{saddles} = 3$

Figure 20: Streakline interpretation of Fig. 17 showing plan-view regional topology $\Sigma\text{nodes} - \Sigma\text{saddles} = 0$ *with three horseshoe vortices.*

7 Flow at the Tip of the Fin

Flow topology of the fin is inferred from available images of surface-oil flow visualisation and smoke visualisation for similar NACA profiles at yaw ($\psi \simeq 10\,^{\circ}$-$12\,^{\circ}$) [13, 14]. In Figs. 21 and 22, the oil streaks track the time-averaged surface-flow bifurcations. In Fig. 23(a), the smoke filaments (illuminated by a 2 mm thick laser-light sheet) capture the instantaneous roll-up. In the simplest interpretation given in Fig. 23(b), the tip vortex (F_{ft}) rolls up on the leeward side; the adjacent half-saddles (S_{ft} and S'_{ft}) satisfy Eq. (3) and are topologically consistent with the positive- and negative-bifurcation lines (B^{+}_{ft} and B^{-}_{ft}) observed on the fin (Fig. 22). As the size of the tip vortex (F_{ft}) increases in the chord-wise (x) direction, the distance between the positive- and negative-bifurcation lines (B^{+}_{ft} and B^{-}_{ft}) also increases. The departure of the tip vortex from the trailing edge of the fin is accompanied by a slight upward deflection of the positive-bifurcation (B^{+}_{ft}) line.

A closer inspection of Fig. 23(a) reveals a pair of counter-rotating eddies (F_{te} and F'_{te}) near the root of the tip vortex (F_{ft}). These eddies are much smaller than the tip vortex and they are rapidly entrained into the tip vortex [14]. In the time-averaged surface-flow pattern, the counter-rotating eddies are embedded in the larger "footprint" of the tip vortex, i.e. the B^{-}_{ft} line — the region of low mean shear indicated by the shaded area in Fig. 22. In the alternate interpretation given in Fig. 23(c), the topology of the fin-tip vortex includes the pair of counter-rotating eddies (F_{te} and F'_{te}). In the region of low mean shear indicated by the shaded area (Fig. 23(c)), the accompanying saddle points (S'_{ft}, S_{te} and S'_{te}) appear as very fine alternating local positive- and negative-bifurcation lines. These alternating bifurcation lines converge as the tip vortex separates from the fin into the downstream flow.

Figure 24 shows that, at the trailing edge of the fin, a change in the yaw angle and/or the (chord) Reynolds number can produce more or less intense mixing of the smoke filaments, but this does not alter the basic topology, i.e. the cross-stream would separate at the tip and roll up to produce a stable focus [13, 14]. From kinematic principles (e.g. [3]), it is possible to deduce some features of the tip vortex downstream of the fin. For example, as the vortex/focus separates from the fin, the two half-saddles (i.e. S_{ft} and S'_{ft}) connect to form a full saddle as shown in Fig. 25. Also, as the focus (F_{ft}) interacts with the surrounding fluid, the vortex stretches and increases in size due to the effect of viscosity. A stretched vortex may contain "limit cycles"; Fig. 25 shows an example of a limit cycle which represents a change from inflow (stable focus) to outflow (unstable focus); the unstable focus, once established, extends downstream to infinity.

8 Vortex Skeleton and Circulation

Earlier sections in this report have identified various features of a submarine flow. These include the hull vortices, the fin-junction vortices and the fin-tip vortex. From this, it is possible to construct a vortex skeleton of the submarine flow by using the first vortex law of Helmholtz [15, 16]. The law states that "*the circulation around a vortex tube*[4] *is constant*" [16]. The inference from this is that the vortex tube (or line) must either form a closed loop, extend to infinity or terminate

[4] A vortex tube is a set of vortex lines passing through a simply-connected surface in space, a vortex line is a line which is everywhere tangent to the local vorticity vector [16].

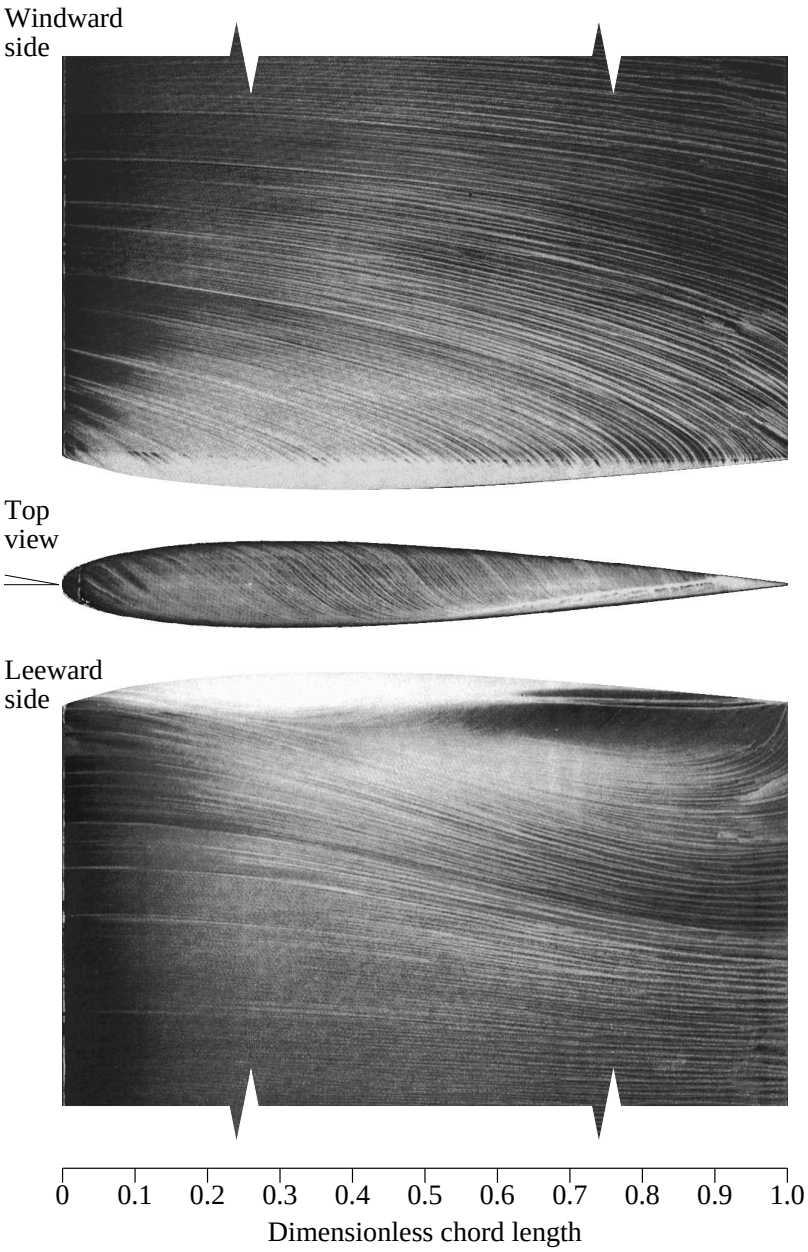

Figure 21: Time-averaged surface-oil flow pattern on a NACA fin [13] (in 3rd-angle orthogonal projection): $\psi \simeq 10^\circ$-12°. The mean flow direction is from left to right.

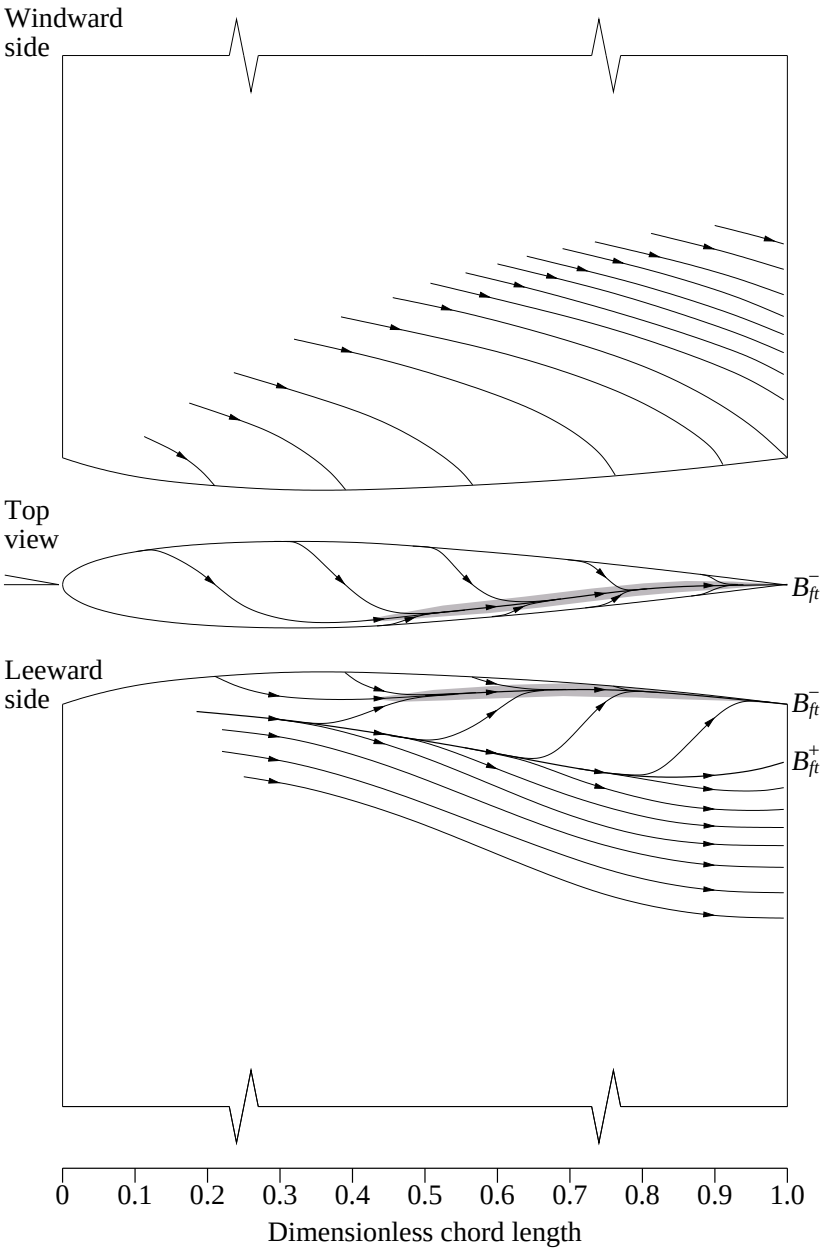

Figure 22: Streakline interpretation of Fig. 21 showing top-view and side-view regional topology $\Sigma\text{nodes} - \Sigma\text{saddles} = 0$. *Shaded area indicates region of low mean shear.*

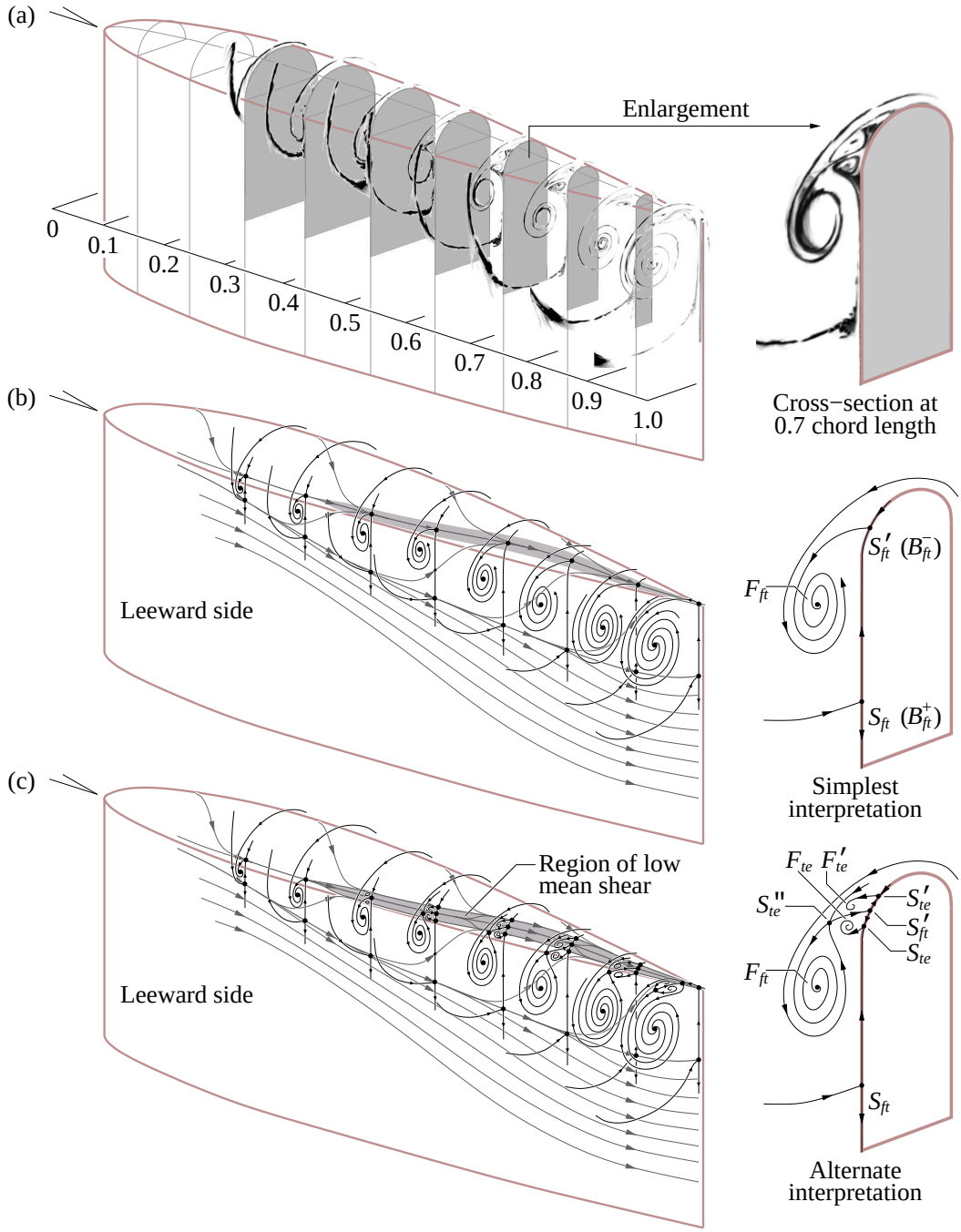

(a)	Cross-section smoke visualisation
(b)	$F_{ft} = \Sigma\text{nodes} = 1$
	$\frac{1}{2}S_{ft} + \frac{1}{2}S'_{ft} = \Sigma\text{saddles} = 1$
(c)	$F_{ft} + F_{te} + F'_{te} = \Sigma\text{nodes} = 3$
	$\frac{1}{2}S_{ft} + \frac{1}{2}S'_{ft} + \frac{1}{2}S_{te} + \frac{1}{2}S'_{te} + S''_{te} = \Sigma\text{saddles} = 3$

Figure 23: Development of a NACA fin-tip vortex for $\psi \simeq 10°$-$12°$. (a) Smoke filaments in air [14]. (b) Interpretation of regional topology ($\Sigma\text{nodes} - \Sigma\text{saddles} = 0$) with the aid of surface streaklines from Fig. 22. (c) Alternate interpretation with a pair of counter-rotating eddies (F_{te} and F'_{te}) at the root of the fin-tip vortex (F_{ft}).

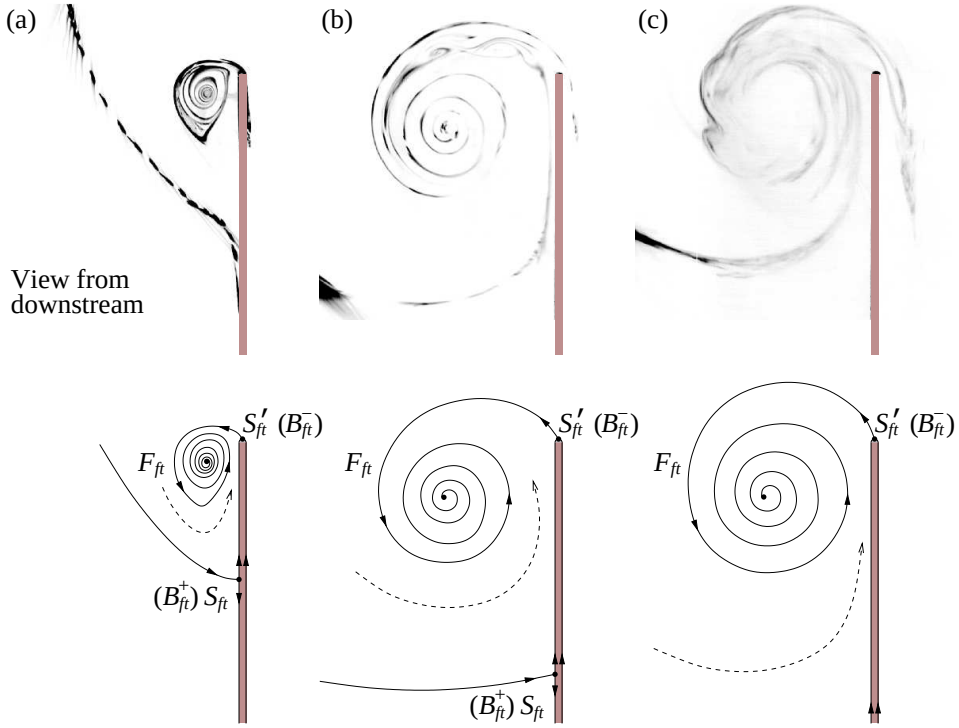

Figure 24: Topology interpretation of the tip vortex aft of a NACA fin; smoke filaments in air [14] with (a) $\psi = 4^\circ$ at the chord Reynolds number $Re_c = c_f U_\infty/\nu = 3000$, (b) $\psi = 12^\circ$ at $Re_c = 3000$ and (c) $\psi = 12^\circ$ at $Re_c = 7000$. The mean flow direction is out of the page.

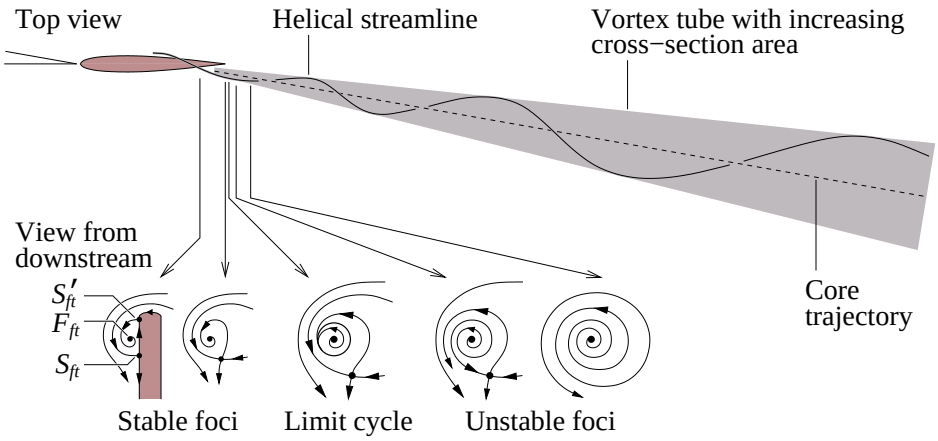

Figure 25: Kinematics of the separated fin-tip vortex (F_{ft}) in the very near field. In cross-section, the flow is viewed from downstream of the fin.

at solid surfaces[5]. For simplicity, the following analysis excludes vortices which may be produced by the control surfaces and/or support structures for the submarine model.

Figure 26 provides an interpretation of the vortex skeleton of the separated flow for small angles of yaw ($0\,^\circ < \psi < 18\,^\circ$). The cross-sections of the vortex skeleton, interpreted from standard topology rules, are shown in Fig. 27. On the leeward side of the submarine, vortex lines form in the vicinity of the nose to produce a pair of counter-rotating hull vortices. For the upper-hull and lower-hull vortices, their centroids are at the vertical locations $z^+_{c,hc}$ and $z^-_{c,hb}$, respectively. At the fin, the leeward flow may be interpreted as a superposition of the free-stream and a U-shaped vortex[6]. This U-shaped vortex (line) consists of three segments: (i) a bound vortex which spans the height of the fin about the aerodynamic center[7] of the fin, connected to (ii) a vortex leg at location $z^+_{c,ft}$ along the tip of the fin and (iii) a vortex leg at location $z^+_{c,hc}$ along the casing.

Figures 26 and 27 show that, on the casing (at location $z^+_{c,hc}$), the rotation sense of the leg of the U-shaped vortex produced by the fin is opposite to that of the upper-hull vortex stretched from the nose, and so there is some cancellation in circulation. Note that fin-junction vortices are present on the casing (at starboard $z^+_{c,fs}$ and port $z^+_{c,fp}$) but they are much smaller than the hull vortices and the fin-tip vortex. For the fin-junction vortices, their size would scale approximately with the displacement thickness[8] of the boundary layer on the casing, i.e. $\sim L/\sqrt{Re_L}$.

Dimensional analysis suggests that circulation (Γ in units of length^2/time) of the flow around the submarine at yaw can be expressed as the dimensionless parameter:

$$\kappa = \frac{\Gamma}{r_m U_\infty \sin(\psi)} \quad \text{for} \quad \sin(\psi) \neq 0, \tag{4}$$

where r_m is the maximum radius of the bare hull and $U_\infty \sin(\psi)$ is the cross-stream velocity. Aft of the hull (or at the tail plane), it is assumed that *all* vorticity is shed from the submarine and gets wrapped up or concentrated into these identifiable longitudinal vortices in the flow field:

$$\text{the hull vortices} \begin{cases} \text{casing} & \kappa^+_{hc} = \dfrac{\Gamma^+_{hc}}{r_m U_\infty \sin(\psi)}, \\ \text{base} & \kappa^-_{hb} = \dfrac{\Gamma^-_{hb}}{r_m U_\infty \sin(\psi)}, \end{cases} \tag{5}$$

$$\text{the fin-tip vortex} \begin{cases} & \kappa^+_{ft} = \dfrac{\Gamma^+_{ft}}{r_m U_\infty \sin(\psi)}, \end{cases} \tag{6}$$

$$\text{and the fin-junction vortices} \begin{cases} \text{starboard} & \kappa^+_{fs} = \dfrac{\Gamma^+_{fs}}{r_m U_\infty \sin(\psi)}, \\ \text{port} & \kappa^-_{fp} = \dfrac{\Gamma^-_{fp}}{r_m U_\infty \sin(\psi)}, \end{cases} \tag{7}$$

where $\kappa^+ > 0$ and $\kappa^- < 0$. In cross-section (Fig. 27), positive circulation is obtained by integrating over area of positive vorticity[9], $\Gamma^+(x) = \iint_A \omega^+_x \, dA > 0$, and negative circulation is obtained by integrating over area of negative vorticity, $\Gamma^-(x) = \iint_A \omega^-_x \, dA < 0$.

[5] Section 4, for example, has shown that a sink focus (F^*_{fl} — a termination point of a vortex line) on the fin is topologically possible.

[6] Surface-flow visualisation has shown evidence of a U-shaped vortex on the leeward side of the fin, see Section 4.

[7] The aerodynamic center point of a symmetrical NACA aerofoil is approximately 25% of the chord from the leading edge. For an angle of attack up to 18 °, the moment coefficient about the quarter-chord point is approximately zero [5].

[8] For example, the displacement thickness of a boundary-layer flow past a flat plate parallel to the flow is given by $\delta^* = 1.721\, x/\sqrt{Re_x}$ [17]; the boundary layer is thin provided that the Reynolds number is large.

[9] The body-axis (x) component of vorticity from the velocity field is defined as $\omega_x = \frac{\partial U_z}{\partial y} - \frac{\partial U_y}{\partial z}$. Vorticity may be calculated based on Stokes theorem, $\omega_x = \Gamma/A = (1/A) \oint_C \vec{U}_{yz} \cdot d\vec{l}$, where the circulation Γ around the boundary C of an area A is equal to the integral of vorticity over the area A.

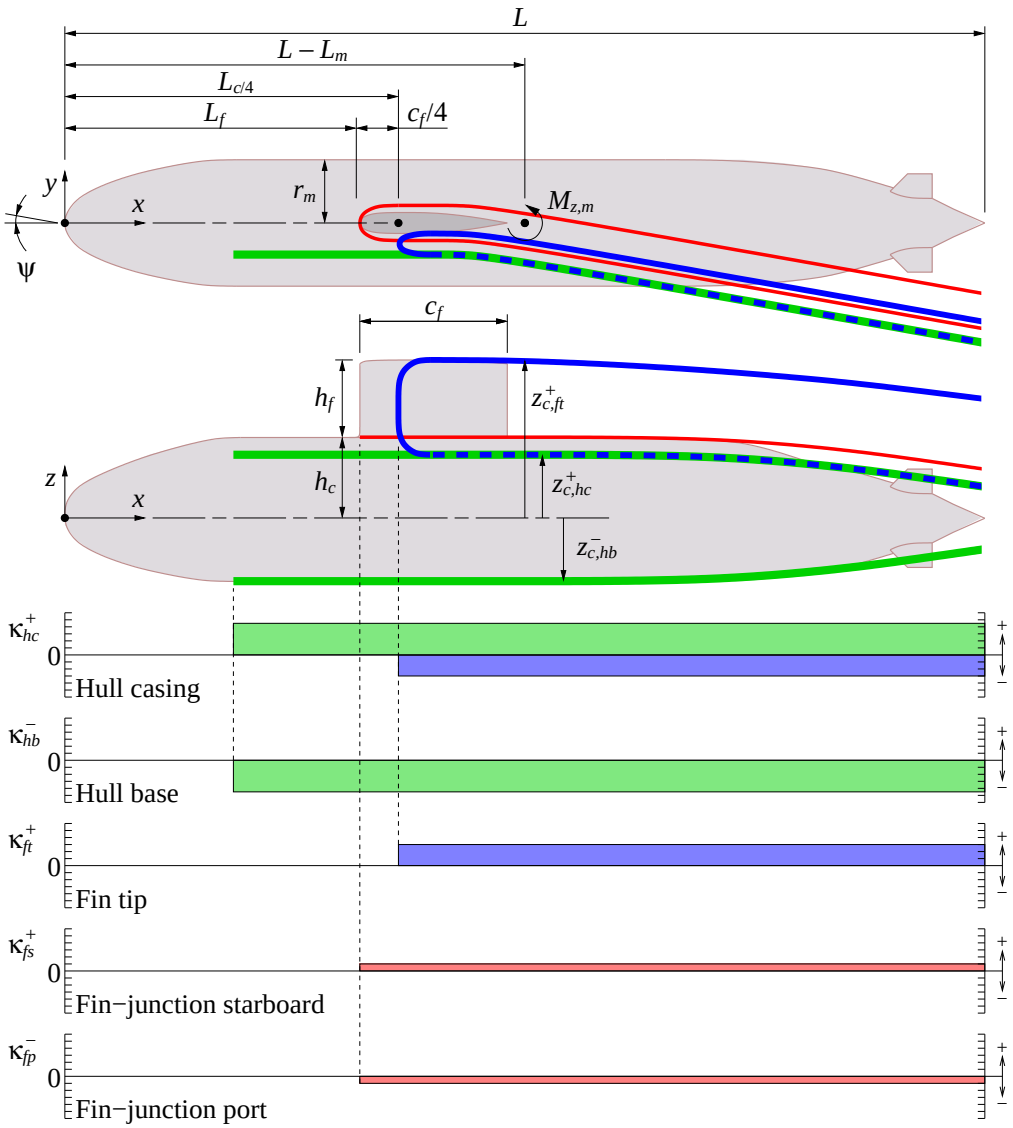

Figure 26: Schematic diagram of vortex lines and circulation around the submarine. The mean flow direction is from left to right. The submarine yaw angle is in the range $0^\circ < \psi < 18^\circ$. The maximum radius of the bare hull is defined as r_m.

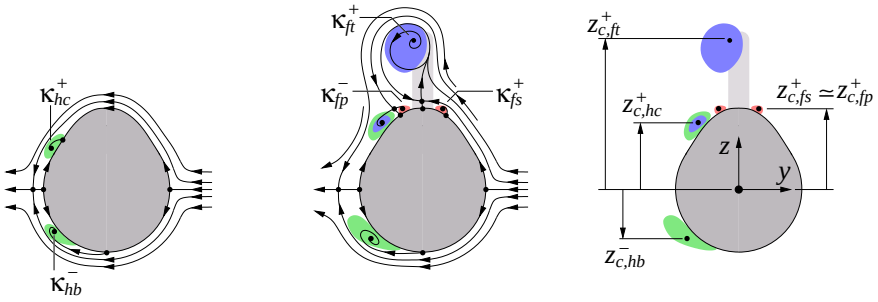

Upstream of fin | Downstream of fin | Coordinate system

Figure 27: Schematic diagram of cross-stream around the submarine. The flow is viewed from the downstream end of the hull; $\kappa^+ > 0$ and $\kappa^- < 0$ denote counter-clockwise and clockwise rotations, respectively; $z_c^+ > 0$ and $z_c^- < 0$ denote the vertical locations of the centroid of vortices in the upper hull and the lower hull, respectively.

An interpretation of circulation around the submarine can be obtained by using the second vortex law of Helmholtz (also known as Kelvin's theorem) [15, 16]. The law states that "*the circulation around a material loop is time-independent*, provided the fluid is inviscid, only subject to potential body forces, and its pressure is a function of density alone" [16]. The inference from this is that an initially irrotational flow (given the three constraints) generates no net circulation; if $\Sigma\Gamma(x, y, z, t{=}0) = 0$, then $\Sigma\Gamma = 0$ for all time (t) throughout space. If a submarine is accelerated from rest in an initially irrotational flow, the net circulation of the flow therefore would remain zero:

$$\Sigma\Gamma(x) = 0 \quad \Rightarrow \quad \Sigma\kappa(x) = \kappa^+_{hc}(x) + \kappa^-_{hb}(x) + \kappa^+_{ft}(x) + \kappa^+_{fs}(x) + \kappa^-_{fp}(x) + \Sigma\kappa_{\text{imag}}(x) = 0, \tag{8}$$

where $\Sigma\kappa_{\text{imag}}(x)$ takes into account the circulation of all mirrored images *inside* the submarine geometry. Note that the fin-junction vortices on the casing are part of the same horseshoe vortex, and so $\kappa^+_{fs}(x) + \kappa^-_{fp}(x) = 0$. At the tail plane $x = L$, Eq. (8) may be simplified to

$$\Sigma\kappa(L) = \kappa^+_{hc}(L) + \kappa^-_{hb}(L) + \kappa^+_{ft}(L) = 0 \tag{9}$$

since $\Sigma\kappa_{\text{imag}}(L) = 0$. In Eq. (9), κ^+_{hc} is the residual circulation due to interactions between the fin U-shaped vortex leg on the casing and the upper-hull vortex stretched from the nose, where $\kappa^+_{hc} < \kappa^+_{ft}$. In the absence of the fin, there is no U-shaped vortex, and so $\kappa^+_{ft} = 0$ and Eq. (9) would reduce to $\kappa^+_{hc} = -\kappa^-_{hb}$. A schematic diagram of the distribution of circulation around the submarine is given in Fig. 26.

To summarise, the constructed vortex skeleton of the flow around the submarine at yaw consists of longitudinal vortices which are stretched downstream to infinity. On the upper hull, a bound vortex connects the longitudinal vortices on the leeward side of the fin (Fig. 26). If the submarine is accelerated from rest in an initially irrotational flow (with the constraints indicated by Kelvin's theorem), the net circulation of these vortices around the submarine would remain zero for all time throughout space.

9 Sway-Force and Yaw-Moment Equations

An understanding of the flow structure (or vortex skeleton) and circulation around the submarine is useful because this can assist with the interpretation of the hydrodynamic forces. In this section, the sway forces are calculated on a part-by-part basis. On the hull, the sway force due to the longitudinal vortices is determined by using the "hydrodynamic-impulse" method described by Jeans et al. [18, 19, 20]. On the fin, the sway force due to the bound vortex is obtained separately by applying the first vortex law of Helmholtz [15, 16]. Where these sway forces act about the mid-ship (or the center of buoyancy) of the submarine, this gives an estimate of the yaw moment.

9.1 Load on the Hull Form

Jeans et al. [18, 19, 20] have shown that, from the slender-body theory [21, 22], the force distribution parallel to the cross-stream (y) direction of a hull at yaw is

$$\mathrm{F}_{y,h} = \rho U_\infty \cos(\psi) \int_0^L di_{y,h}(x) \tag{10}$$

where $i_{y,h}(x)$ is the hydrodynamic impulse in the cross-stream (y) direction of the hull with cross-section area $A_h(x)$:

$$i_{y,h}(x) = \int_{-\infty}^{\infty}\int_{-\infty}^{\infty} (\omega_x z)\, dydz - U_\infty \sin(\psi)\, A_h(x). \tag{11}$$

On the right side of Eq. (11), the first term is a moment of vorticity. Aft of the hull, the second term is zero given that $A_h(L) = 0$.

Since the moment of vorticity depends on the vertical distribution of longitudinal vortices (i.e. $\omega_x z$), it is possible to model Eq. (11) by using the vortex skeleton described in Section 8. To begin, let the hydrodynamic impulse be defined by the system of vortices at the tail plane $x = L$:

$$\begin{aligned} i_{y,h}(L) &= r_m U_\infty \sin(\psi) \times \Sigma(\kappa\, z_{c,\mathrm{aft}}) \\ &= r_m U_\infty \sin(\psi) \times \left(\kappa^+_{hc} z^+_{c,hc,\mathrm{aft}} + \kappa^-_{hb} z^-_{c,hb,\mathrm{aft}} + \kappa^+_{ft} z^+_{c,ft,\mathrm{aft}}\right) \neq 0, \end{aligned} \tag{12}$$

where the circulation parameter κ and the vertical centroid location $z_{c,\mathrm{aft}}$ of each tail-plane vortex are assumed to be roughly constant for limited yaw angles in the range $0^\circ < \psi < 18^\circ$. Eq. (12) excludes the much smaller fin-junction vortices because they are part of the same horseshoe vortex formed on the hull casing and their moments of vorticity would approximately cancel (i.e. $\kappa^+_{fs} z^+_{c,fs} + \kappa^-_{fp} z^+_{c,fp} \simeq 0$, see Figs. 26 and 27). For the hull vortices and the fin-tip vortex, they are asymmetrically distributed about the hull and their circulations are different, and so the net moment of vorticity due to these vortices would not equal to zero. *If the net moment of vorticity is zero, there would be no sway force acting on the submarine.*

From integrating Eq. (10) and substituting Eq. (12) into the expression, this yields

$$\mathrm{F}_{y,h} = \rho U_\infty^2 r_m \cos(\psi)\sin(\psi) \times \left(\kappa^+_{hc} z^+_{c,hc,\mathrm{aft}} + \kappa^-_{hb} z^-_{c,hb,\mathrm{aft}} + \kappa^+_{ft} z^+_{c,ft,\mathrm{aft}}\right). \tag{13}$$

The mid-ship yaw moment due to this force may be expressed as

$$\mathrm{M}_{z,h,m} = K_h \times \mathrm{F}_{y,h} L_m, \tag{14}$$

where L_m is the distance from the tail plane to mid-ship and K_h is a coefficient of proportionality.

9.2 Load on the Fin

In Section 8, the wake of the fin is interpreted as a superposition of the free-stream and a U-shaped vortex. In reality, the wake of the fin would contain infinitely many instantaneous U-shaped-like vortex lines. These vortex lines are spread along the fin to form a vertical vortex sheet with local strength $\Gamma_{fb}(z)$; the sway force acting on the aerodynamic center of the fin is given by the expression:

$$\mathrm{F}_{y,f} = \rho U_\infty \int_{h_c}^{h_c+h_f} \Gamma_{fb}(z)\, dz, \tag{15}$$

where h_c is the height of the casing and h_f is the height of the fin measured from the casing (Fig. 26). By applying the first vortex law of Helmholtz [15, 16], the circulation produced by the fin bound vortex is equal to the circulation produced by the fin-tip vortex, i.e.

$$\Gamma_{fb} = \Gamma_{ft}, \tag{16}$$

and so Eq. (15) may be recast as

$$\mathrm{F}_{y,f} = \rho U_\infty^2\, r_m \sin(\psi) \times K_f \kappa_{ft}^{+} h_f, \tag{17}$$

where K_f is a coefficient of proportionality and κ_{ft}^{+} is defined by Eq. (6). The mid-ship yaw moment due to this force may be expressed as

$$\mathrm{M}_{z,f,m} = \mathrm{F}_{y,f} \times \left(L - L_m - L_{c/4}\right), \tag{18}$$

where $L_{c/4} = L_f + c_f/4$ is the distance from the submarine nose to the quarter-chord point of the fin (see Fig. 26); for the Joubert geometry, $L_f/L = 0.31$, $c_f/L = 0.16$ and $L_{c/4}/L = 0.35$.

9.3 Load on the Overall Geometry

The total sway force acting on the submarine is obtained by adding the sway forces given by Eqs. (13) and (17):

$$\begin{aligned} \mathrm{F}_y &= \mathrm{F}_{y,h} + \mathrm{F}_{y,f} \\ &= \rho U_\infty^2 L\, r_m \times \left[K_1 \cos(\psi) + K_f K_2\right] \sin(\psi) \end{aligned} \tag{19}$$

and the total yaw moment about the mid-ship is obtained by adding the yaw moments given by Eqs. (14) and (18):

$$\begin{aligned} \mathrm{M}_{z,m} &= \mathrm{M}_{z,h,m} + \mathrm{M}_{z,f,m} \\ &= \rho U_\infty^2 L^2\, r_m \times \left[\frac{L_m}{L} K_h K_1 \cos(\psi) + \left(1 - \frac{L_m}{L} - \frac{L_{c/4}}{L}\right) K_f K_2\right] \sin(\psi), \end{aligned} \tag{20}$$

where the non-dimensionalised moments of vorticity are given by the expressions:

$$K_1 = \kappa_{hc}^{+} \frac{z_{c,hc,\mathrm{aft}}^{+}}{L} + \kappa_{hb}^{-} \frac{z_{c,hb,\mathrm{aft}}^{-}}{L} + \kappa_{ft}^{+} \frac{z_{c,ft,\mathrm{aft}}^{+}}{L}, \tag{21}$$

$$K_2 = \kappa_{ft}^{+} \frac{h_f}{L}. \tag{22}$$

From non-dimensionalising Eqs. (19) and (20) by the free-stream velocity U_∞ and the submarine length L, this gives the sway-force and mid-ship yaw-moment coefficients:

$$\begin{aligned} C_{\mathrm{F}_y} &= \mathrm{F}_y \Big/ \left(\frac{1}{2}\rho U_\infty^2 L^2\right) \\ &= \left[\frac{K_1}{R}\cos(\psi) + \frac{K_f K_2}{R}\right]\sin(\psi), \end{aligned} \tag{23}$$

$$\begin{aligned} C_{\mathrm{M}_z} &= \mathrm{M}_{z,m} \Big/ \left(\frac{1}{2}\rho U_\infty^2 L^3\right) \\ &= \left[\frac{L_m}{L}\frac{K_h K_1}{R}\cos(\psi) + \left(1 - \frac{L_m}{L} - \frac{L_{c/4}}{L}\right)\frac{K_f K_2}{R}\right]\sin(\psi), \end{aligned} \tag{24}$$

where $R = L/(2r_m)$ is the slenderness ratio of the bare hull; at mid-ship, $L_m/L = 1/2$.

10 Circulation, Force and Moment: A Review of Data

This section is set out to find the model coefficients (K_1, K_2, K_f and K_h in Eqs. (21)-(24)) for the Joubert submarine geometry. To determine the model coefficients, this requires force and moment data (C_{F_y}, C_{M_z}) and circulation data (κ, z_c).

At the time of writing, the author knows of two cases where circulation, force and moment data have been published; they are from RANS CFD[10] simulations for bare hulls "DRDC-STR" and "Series 58-4621" [18, 19, 20]. On the basis of geometric similarity (i.e. hulls with similar slenderness ratios, see Fig. 28), it seems likely that these bare hulls and the Joubert hull would also produce similar circulation of cross-stream vortices. Given that the Joubert fin has the shape of a rounded-tip NACA-0015 aerofoil, circulation of the fin-tip vortex may be estimated by using available data for a stand alone NACA-0015 aerofoil[11].

10.1 Scaling of Circulation

Figures 29 and 30 provide a review summary of circulation data for the bare hulls DRDC-STR and Series 58-4621 and for the aerofoil NACA-0015.

The bare-hull parameters:

$$\kappa = \frac{\Gamma}{r_m U_\infty \sin(\psi)} = 2R\sqrt{\frac{A_p}{L^2}\tan(\psi)} \times \Gamma^*_{A_p}, \tag{25}$$

$$\frac{z_c}{L} = \sqrt{\frac{A_p}{L^2}\tan(\psi)} \times z^*_{c,A_p} \tag{26}$$

[10] The RANS CFD (Reynolds averaged Navier Stokes computational fluid dynamics) are calculated using the SST (shear stress transport) "k-ω" turbulence model, see [18, 19, 20].

[11] Note that, for a fin-and-hull combination, the sway force may differ from that of a stand alone fin because of interference effects, e.g. [25, 26]. For ease of analysis, possible fin-and-hull interference effects are absorbed by the coefficient of proportionality K_f introduced by Eq. (17).

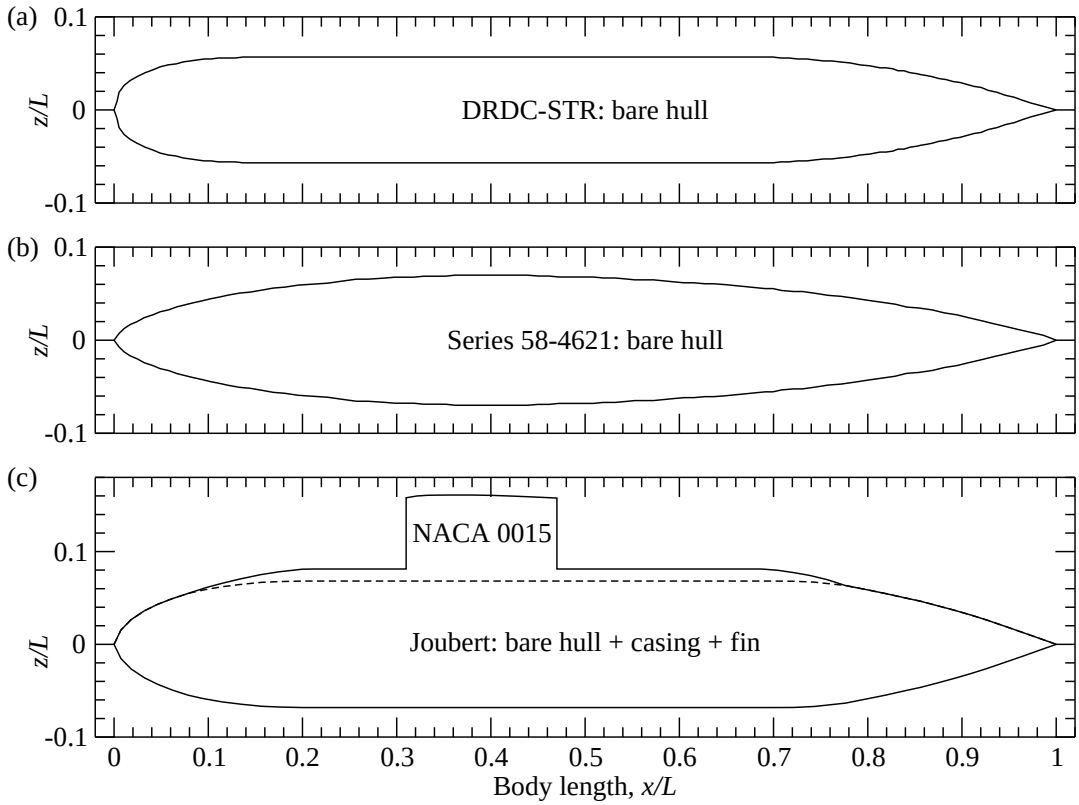

Hull form	$R = L/(2r_m)$	$L_{c/4}/L$	c_f/L	h_f/L
DRDC-STR: bare hull	8.75	n/a	n/a	n/a
Series 58-4621: bare hull	7.34	n/a	n/a	n/a
Joubert: bare hull + casing + fin	7.3	0.35	0.16	0.08

Figure 28: Examples of generic hull forms: (a) Defense Research and Development Canada — Static Test Rig, (b) Naval Surface Warfare Center Carderock Division Series 58-4621, and (c) Defence Science and Technology Group — the submarine shape by Joubert. Geometric parameters are defined in Fig. 26; n/a = *not applicable.*

are plotted as functions of body length (x/L) in Fig. 29 and as functions of yaw angle (ψ) in Fig. 30, where the values for the dimensionless groups:

$$\Gamma^*_{A_p} = \frac{\Gamma}{U_\infty \sin(\psi)\sqrt{A_p \tan(\psi)}}, \tag{27}$$

$$z^*_{c,A_p} = \frac{z_c}{\sqrt{A_p \tan(\psi)}} \tag{28}$$

are taken from RANS CFD simulation [20]. For both DRDC-STR and Series 58-4621, the non-dimensionalised planform area, A_p/L^2, is approximately 0.1.

In Figs. 29 and 30, the fin parameters are defined as

$$\kappa = \frac{\Gamma}{r_m U_\infty \sin(\psi)} = \frac{c_f}{r_m \sin(\psi)} \times \Gamma^*_c, \tag{29}$$

$$\frac{z_c}{L} = \frac{c_f}{L} \times z^*_{c,c}, \tag{30}$$

where c_f is the chord length; the values for the dimensionless groups:

$$\Gamma^*_c = \frac{\Gamma}{U_\infty c_f}, \tag{31}$$

$$z^*_{c,c} = \frac{z_c}{c_f} \tag{32}$$

are taken from various wind-tunnel experiments [7, 27, 28] and RANS CFD simulation [29]. In Figs. 29 and 30, the NACA-0015 aerofoil data (κ, z_c/L) are plotted using the ratios $c_f/L = 0.16$ and $c_f/r_m = (c_f/L) \times 2R = 2.34$ for the Joubert submarine geometry (see Fig. 28). The leading edge of the Joubert fin is at $x/L = 0.31$.

10.2 Interpretation of Circulation Data

In Figs. 29 and 30, κ for the bare hulls is the circulation magnitude of the counter-rotating vortices (i.e. $\kappa_{hc} = \kappa_{hb}$); for the fin, κ is the total strength of the tip vortex (i.e. κ_{ft}). For each structure, its vertical centroid location z_c is measured from the body (x) axis of the hull (see Figs. 26 and 27).

Figure 29(a) shows that circulation increases with increasing streamwise distance from the leading edge of both the hull and the fin. The rise in circulation is most likely due to the summation of circulation contributed by an increasing number of vortex lines formed along the submarine. Figure 31 shows a schematic diagram of possible distribution of vortex lines, where (finer) upstream vortex lines eventually roll up or grouped together to form (thicker) downstream vortex tubes.

From inspection of Fig. 29(b), it is possible to infer the location of the vortices at the tail plane. For example, the vertical distance between the centroids of the hull vortices does not exceed the maximum diameter of the hull, i.e.

$$\frac{z^+_{c,hc,\text{aft}} - z^-_{c,hb,\text{aft}}}{L} = \gamma_h \frac{1}{R}, \qquad 0 < \gamma_h < 1, \tag{33}$$

and the vertical location of the tip vortex does not exceed the height of the fin, i.e.

$$\frac{z^+_{c,ft,\text{aft}}}{L} = \gamma_f \left(\frac{1}{2R} + \frac{h_f}{L} \right), \qquad 0 < \gamma_f < 1, \tag{34}$$

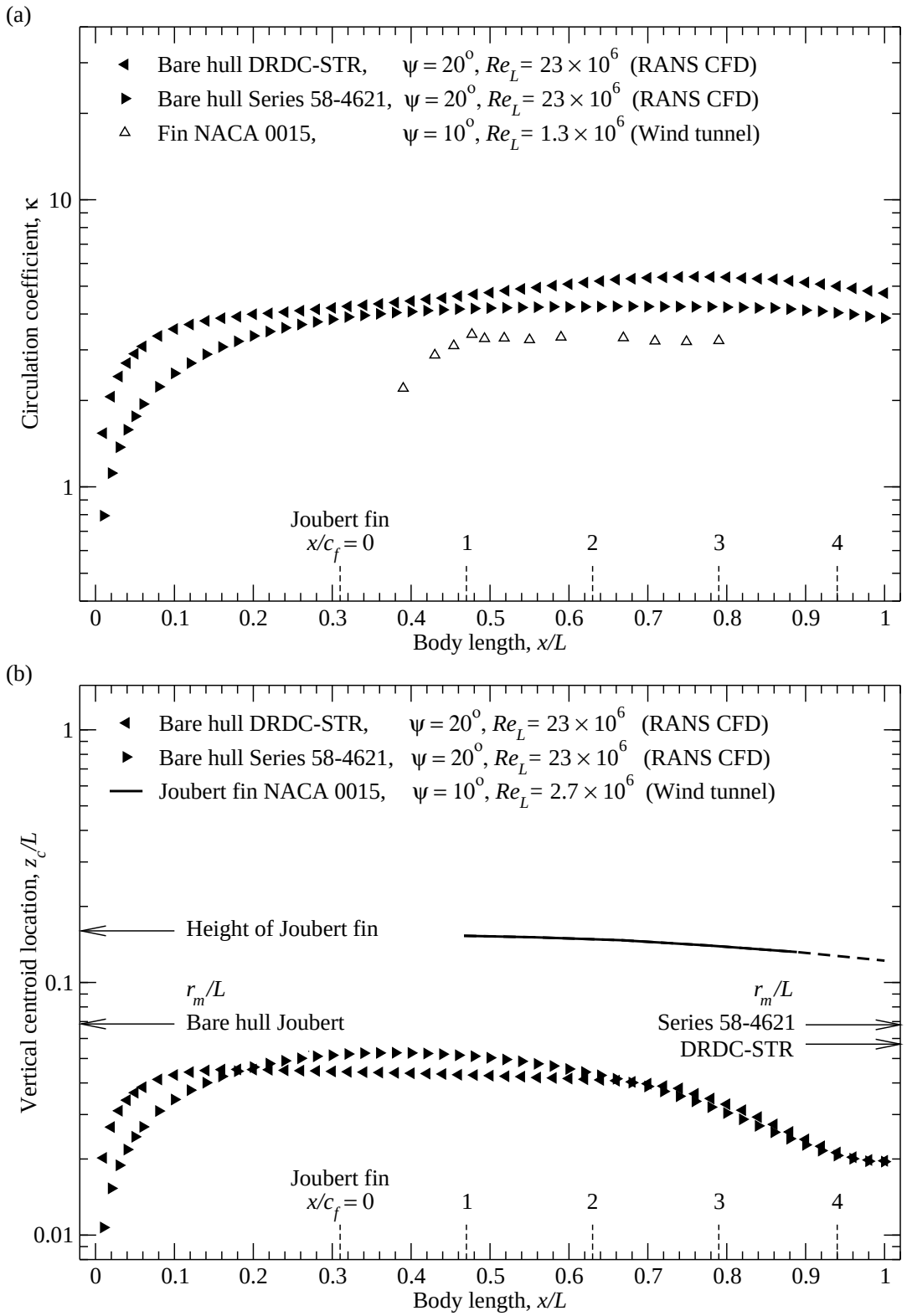

Figure 29: Circulation and location of vortices along the submarine. Eqs. (25)-(32) are used to plot the data; bare hull "◄", "►" [20]; fin "——" [7], "△" [27].

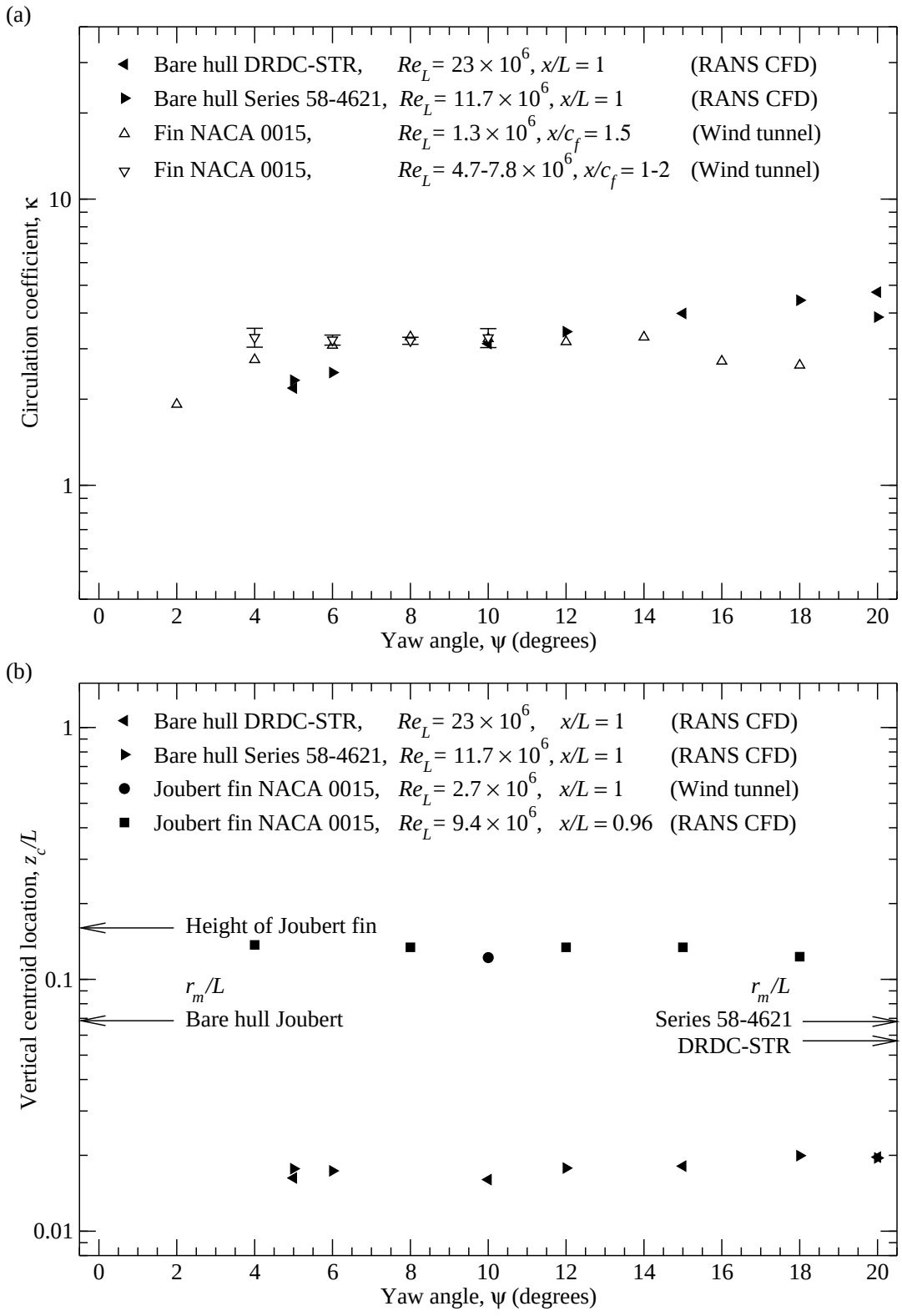

Figure 30: Circulation and location of vortices as functions of ψ. Eqs. (25)-(32) are used to plot the data; bare hull "◄", "►" [20]; fin "●" [7], "△" [27], "▽" [28], "■" [29].

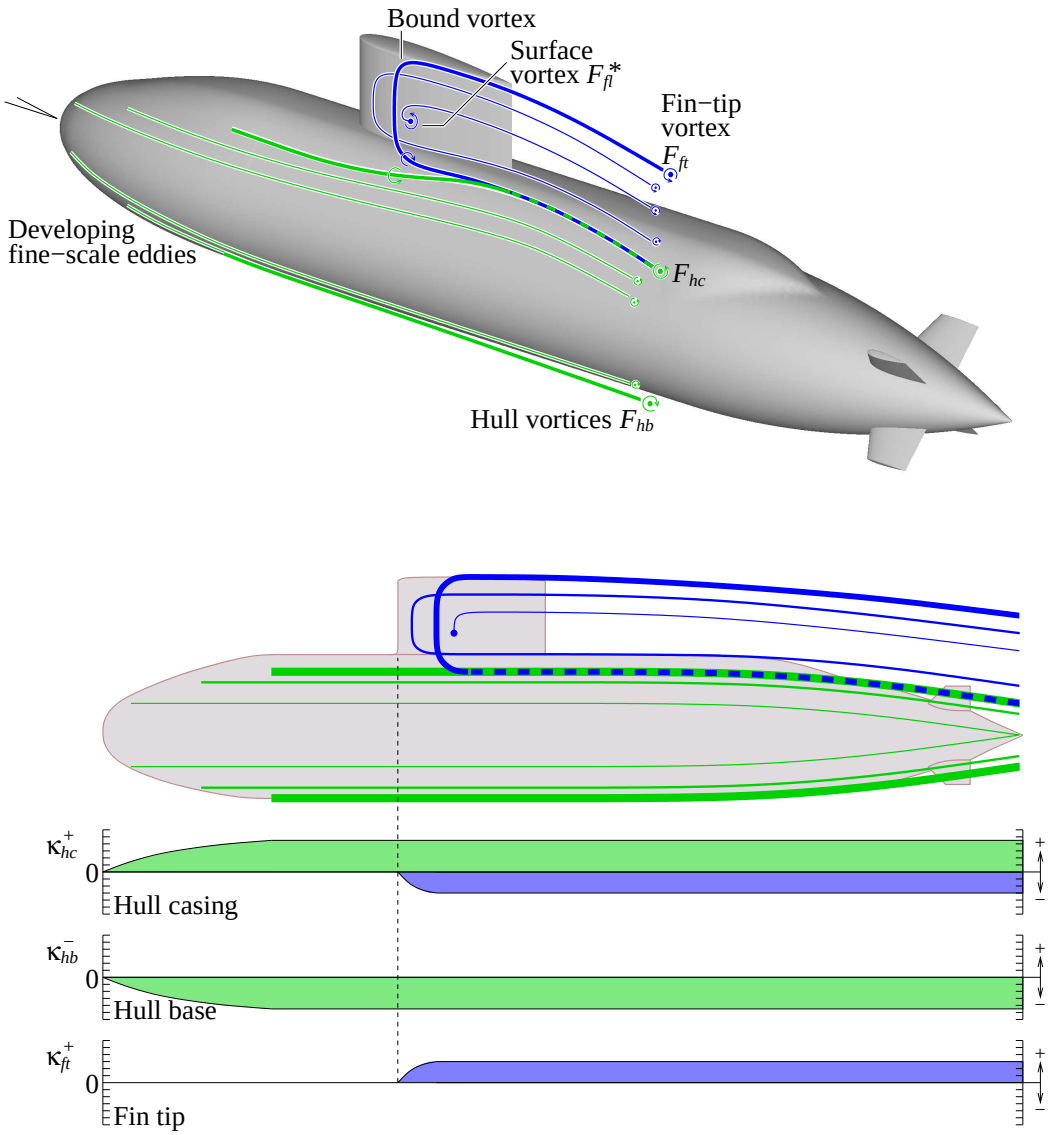

Figure 31: Possible distribution of vortex lines and circulation around the submarine, after Fig. 26. The mean flow direction is from left to right. For clarity, the junction vortices around the fin are not included.

where γ_h and γ_f are coefficients of proportionality for the hull vortices and the fin vortex, respectively. For a hull with an approximately round cross-section, this gives $z^+_{c,hc,\text{aft}} \simeq -z^-_{c,hb,\text{aft}}$, and so by substituting Eqs. (33) and (34) into Eq. (21) this yields

$$K_1 = \gamma_h \frac{1}{2R}(\kappa^+_{hc} - \kappa^-_{hb}) + \gamma_f \left(\frac{1}{2R} + \frac{h_f}{L}\right) \kappa^+_{ft}, \tag{35}$$

which relates coefficient K_1 to the shape of the submarine.

It should be noted that Eq. (35) is only an approximate for a narrow range of yaw angles. For example, Fig. 30 shows that with increasing yaw angle (ψ), there is a slight increase in circulation (κ) for the vortices shed by the hull and the fin; the vertical locations of these vortices (z_c) are approximately constant. As yet, the present analytical model does not take into account detailed variations in the flow (circulation) with changing yaw angle[12].

10.3 Calibrating the Force and Moment Equations

Section 9 has established that the equations for the sway-force and yaw-moment coefficients are of the forms:

$$C_{\text{F}_y} = [A\cos(\psi) + B]\sin(\psi), \tag{36}$$
$$C_{\text{M}_z} = [C\cos(\psi) + D]\sin(\psi), \tag{37}$$

where

$$A = \frac{K_1}{R}, \tag{38}$$
$$B = \frac{K_f K_2}{R}, \tag{39}$$
$$C = \frac{L_m}{L} K_h A, \tag{40}$$
$$D = \left(1 - \frac{L_m}{L} - \frac{L_{c/4}}{L}\right) B. \tag{41}$$

For yaw moment about the mid-ship, $L_m/L = 1/2$. In Fig. 28, the hull forms are shown with and without a fin. In the absence of a fin, K_f and K_2 (and hence B and D) are equal to zero, and K_1 and K_h (and hence A and C) are solved simultaneously by least-squares fitting to force and moment (C_{F_y}, C_{M_z}) data. With a fin, K_1 and K_2 are obtained by solving Eqs. (35) and (22) respectively, and then the remaining coefficients K_f and K_h are solved simultaneously by curve fitting to force and moment (C_{F_y}, C_{M_z}) data.

10.3.1 The "DRDC-STR" and "Series 58-4621" Bare Hulls

In Figs. 32 and 33, the force and moment coefficients are plotted as functions of yaw angle (ψ) for the bare hulls DRDC-STR and Series 58-4621. The data are from measurements in a wind tunnel

[12] At very small yaw angles ($0^\circ \le \psi \ll 10^\circ$), the flow is nearly symmetrical about the mirror plane of the submarine with negligible leeward vortices produced along the hull (see Section 4). At larger yaw angles ($\psi \gtrsim 10^\circ$), strong circulation produces a reattachment node on the leeward face of the fin; further increasing the yaw angle can produce greater separation in the vicinity of the nose leading to the Werlé-Legendre horn vortices (see Section 5).

and in a towing tank, and from RANS CFD simulations, see [20]. Inspection shows that, due to scatter, there is little discernible difference between the data for DRDC-STR and Series 58-4621; the data (◁, ◀, ▷, ▶) in the range $5^\circ \le \psi \le 15^\circ$ fall on

$$C_{F_y} = 0.015 \cos(\psi) \sin(\psi), \tag{42}$$

$$C_{M_z} = 0.011 \cos(\psi) \sin(\psi), \tag{43}$$

with root-mean-square (r.m.s.) errors of 26% and 8%, respectively.

From Eq. (9), $\Sigma\kappa = \kappa^+_{hc} + \kappa^-_{hb} = 0$ since $\kappa^+_{ft} = 0$ in the absence of the fin. So, by substituting Eq. (38) into Eq. (35) with $\kappa^+_{ft} = 0$ and rearranging the expression, this gives the circulation of the bare-hull vortices:

$$\frac{\kappa^+_{hc} - \kappa^-_{hb}}{2} = \frac{A \times R^2}{\gamma_h} \quad \Rightarrow \quad \kappa^+_{hc} = -\kappa^-_{hb} = \frac{A \times R^2}{\gamma_h}, \tag{44}$$

where $A = 0.015$ from Eq. (42).

Inspection of Fig. 30(b) shows that, at $x = L$, the vertical location of the bare-hull vortices is approximately one-third of the maximum radius of the bare hull, i.e. $\gamma_h = 0.34$ for DRDC-STR and $\gamma_h = 0.28$ for Series 58-4621. Solving Eq. (44) yields $\kappa^+_{hc} = -\kappa^-_{hb} = 0.015 \times 8.75^2/0.34 = 3.4$ for DRDC-STR and $\kappa^+_{hc} = -\kappa^-_{hb} = 0.015 \times 7.34^2/0.28 = 2.9$ for Series 58-4621. These predicted values of κ are in agreement with the bare-hull simulation data (◀, ▶) shown in Fig. 30(a) for the range $5^\circ \le \psi \le 15^\circ$.

10.3.2 The "Joubert" Hull Form without a Fin

Figures 34 and 35 show the force and moment coefficients plotted as functions of yaw angle (ψ) for the Joubert submarine[13] starting with a bare hull, then adding the casing and the fin. In the range $5^\circ \le \psi \le 15^\circ$, the Joubert bare-hull data (○) fall on

$$C_{F_y} = 0.036 \cos(\psi) \sin(\psi), \tag{45}$$

$$C_{M_z} = 0.014 \cos(\psi) \sin(\psi), \tag{46}$$

with r.m.s. errors of 20% and 7%, respectively. With the casing, the force and moment coefficients are slightly larger and the experimental data (+) fall on

$$C_{F_y} = 0.042 \cos(\psi) \sin(\psi), \tag{47}$$

$$C_{M_z} = 0.017 \cos(\psi) \sin(\psi), \tag{48}$$

with r.m.s. errors of 21% and 7%, respectively. Note that the casing adds to the height of the hull and so it seems likely that the vertical distance between the hull vortices, i.e. γ_h as defined in Eqs. (33) and (44), would also increase with the height of the hull. A plot of Eq. (44) in Fig. 36(a) shows the effect of increasing γ_h on the circulation (κ^+_{hc}, κ^-_{hb}) for the Joubert bare hull without the casing ($A = 0.036$) and with the casing ($A = 0.042$).

[13] The measurements are for $Re_L = 5.2 \times 10^6$ tested in the Defence Science and Technology Group low-speed wind tunnel [23, 24]. They are obtained by using a 6-component strain-gauge balance fitted inside the submarine via a single-pylon support on a turntable. The measurement uncertainties for C_{F_y} and C_{M_z} are 0.15×10^{-3} and 0.03×10^{-3}, respectively [24].

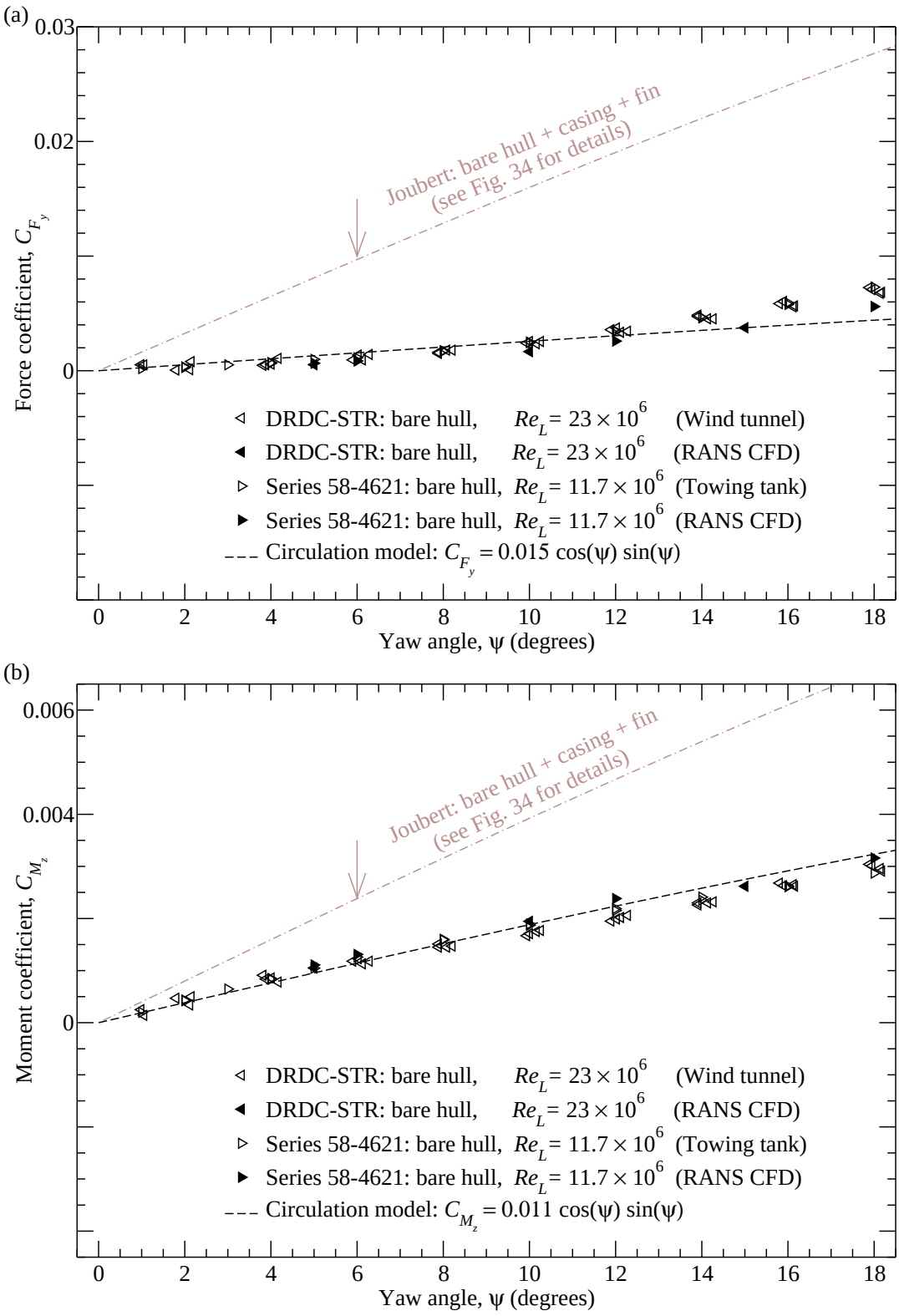

Figure 32: Force and moment coefficients as functions of yaw angle for generic bare hulls; a curve fit of Eqs. (23) and (24) on the review data from [20].

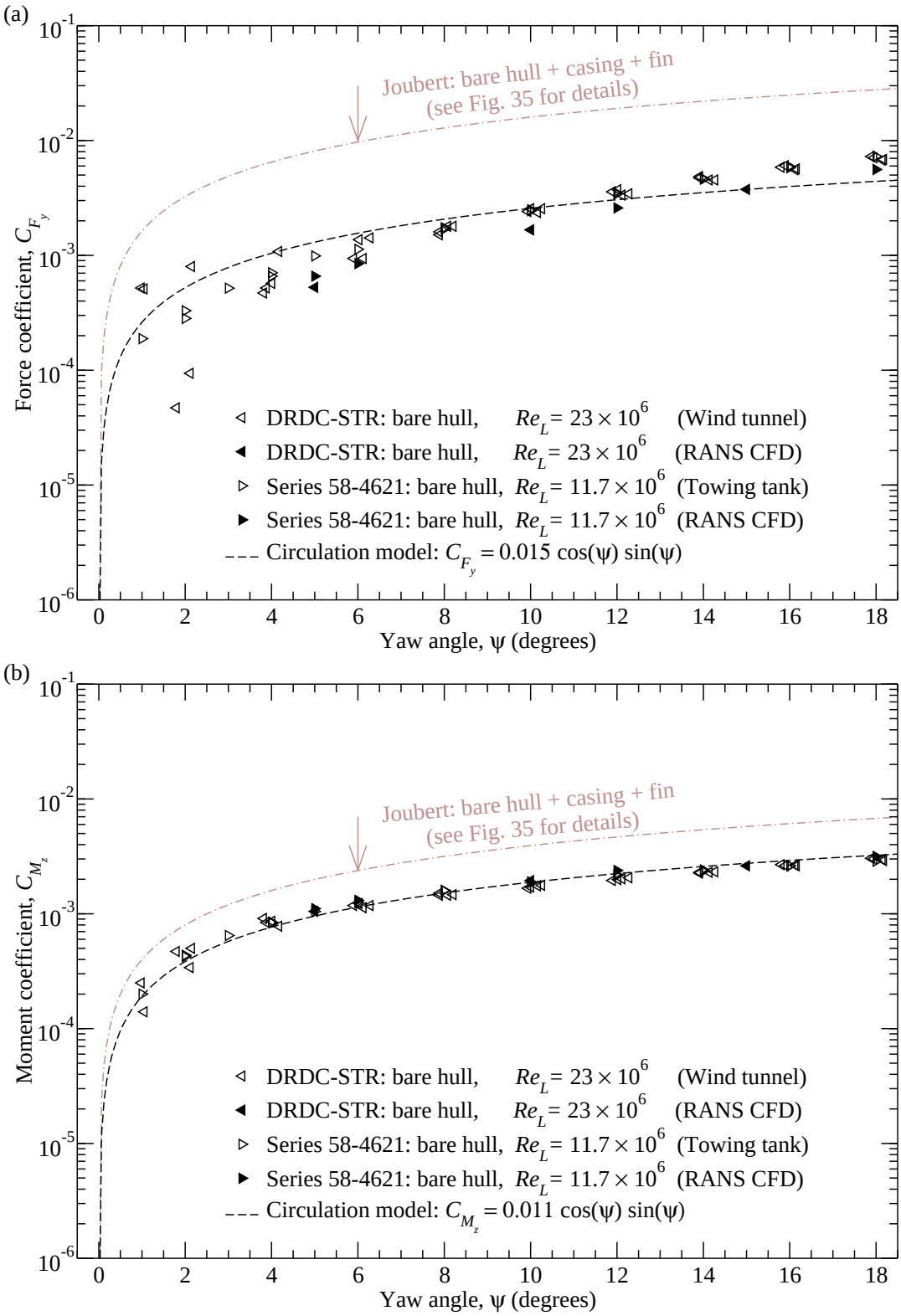

Figure 33: Logarithmic-linear plot of Fig. 32.

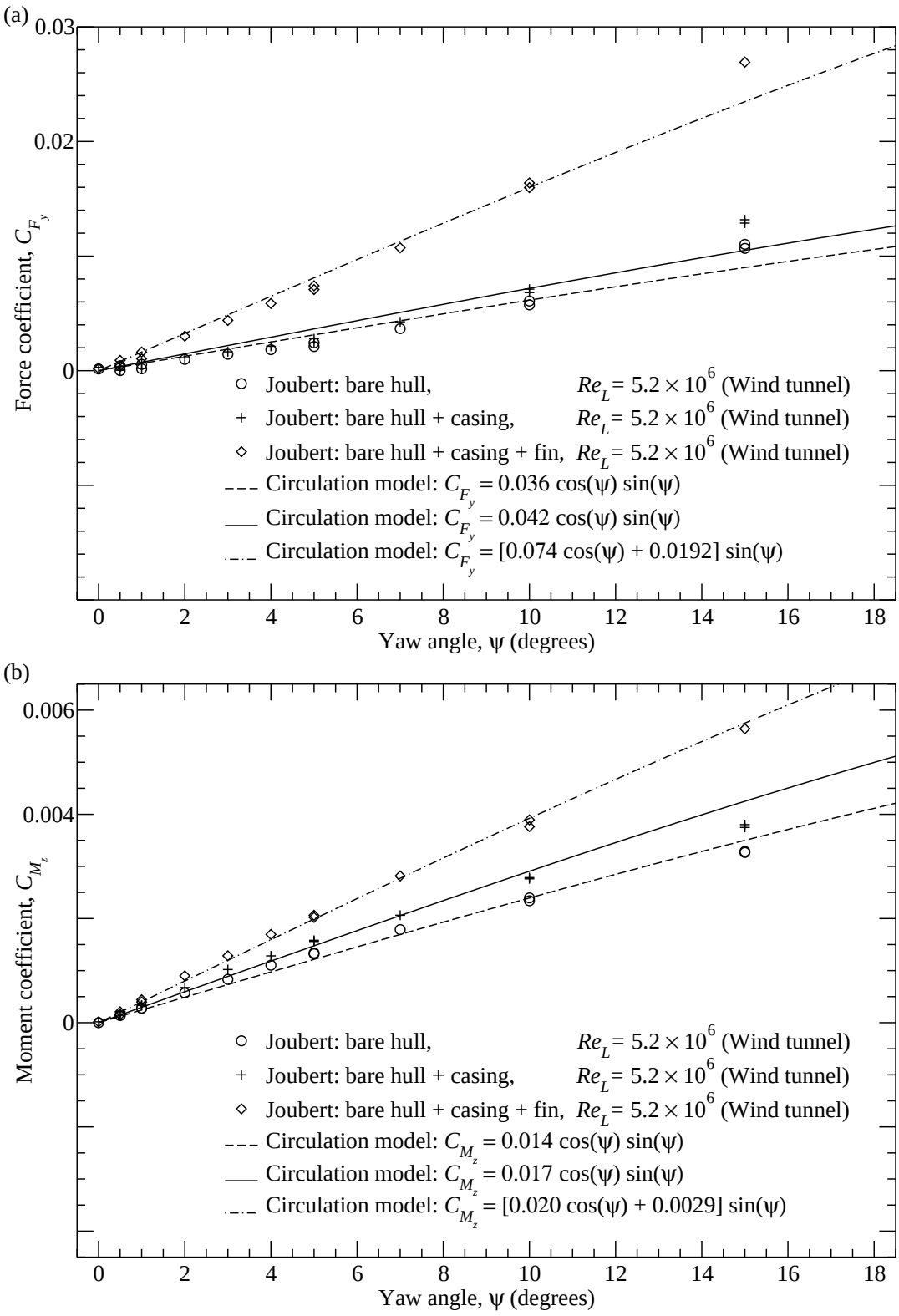

Figure 34: Force and moment coefficients as functions of yaw angle for the generic Joubert hull form; a curve fit of Eqs. (23) and (24) on the experimental data from [23, 24].

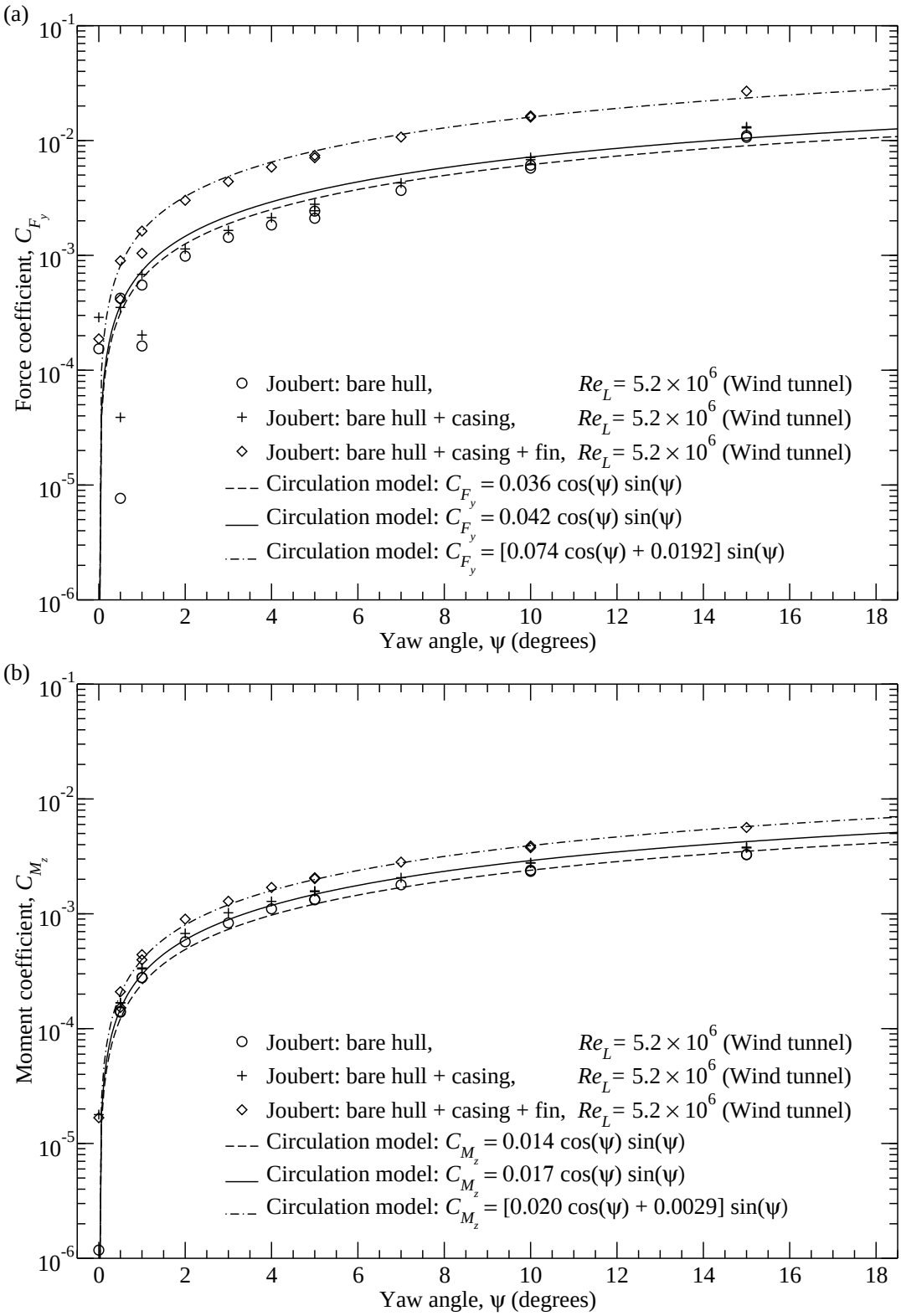

Figure 35: Logarithmic-linear plot of Fig. 34.

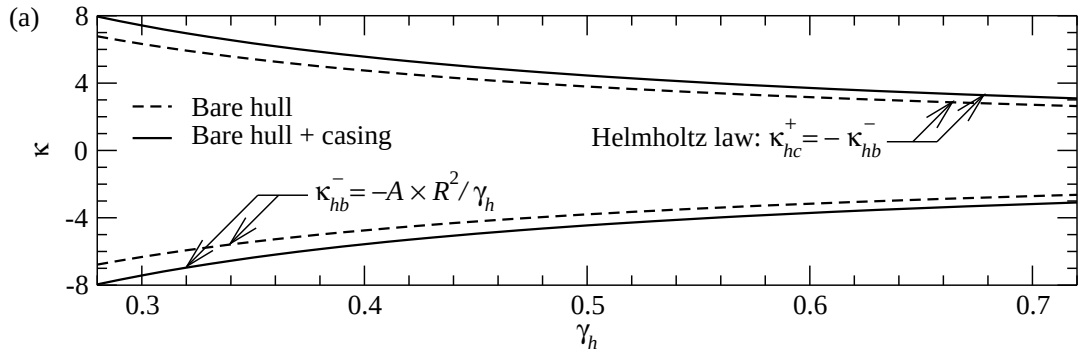

Joubert geometry	K_1	K_h	A	C
Bare hull	0.263	0.778	0.036	0.014
Bare hull + casing	0.307	0.810	0.042	0.017

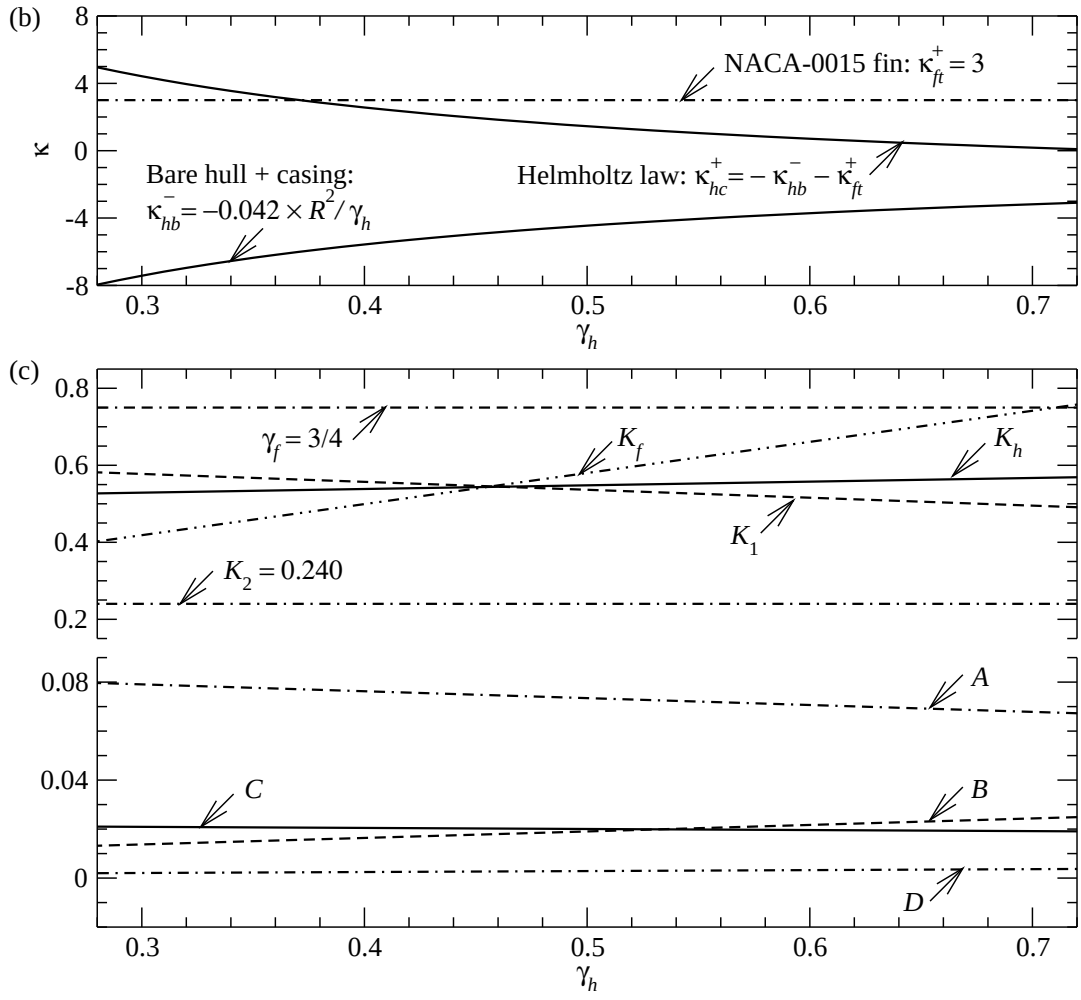

Figure 36: Summary of least-squares fitting to force and moment data for the Joubert hull form using Eqs. (22), (35) and (36)-(41). (a) Bare hull with and without casing. (b, c) Bare hull with casing and fin. $R = 7.3$, $L_{c/4} = 0.35$, $h_f/L = 0.08$ and $L_m/L = 1/2$.

10.3.3 The "Joubert" Hull Form with a Fin

To curve fit the fin-appended data ($\diamond$) in Figs. 34 and 35, the process begins by solving K_2 in Eq. (22) and K_1 in Eq. (35). This requires information on the fin-tip vortex (κ^+_{ft}, γ_f) and the hull vortices (κ^-_{hb}, κ^+_{hc} and γ_h); the information is obtained as follows.

1. Inspection of Fig. 30 shows that, for the range $5^\circ \le \psi \le 15^\circ$, the fin-tip vortex has approximately constant circulation $\kappa^+_{ft} = 3$ and is located at about three-quarter of the distance from the center-line of the hull to the top of the fin, i.e. $\gamma_f = 3/4$. By using Eq. (22), $K_2 = \kappa^+_{ft} \times (h_f/L) = 3 \times 0.08 = 0.240$.

2. Note that no alteration is made to the lower hull, therefore circulation on the lower hull is assumed to be unchanged, and so $\kappa^-_{hb} = -A \times R^2/\gamma_h$ from Eq. (44), where $A = 0.042$ from Eq. (47).

3. Since the flow field on the upper hull is dominated by the fin-tip vortex, much of the circulation on the upper hull is contributed by this vortex with the constraints:

$$\kappa^+_{ft} > \kappa^+_{hc} > 0 \quad \text{and} \quad \frac{A \times R^2}{2\kappa^+_{ft}} < \gamma_h < \frac{A \times R^2}{\kappa^+_{ft}}, \tag{49}$$

   where $A = 0.042$, $R = 7.3$ and $\kappa^+_{ft} = 3$ specify the range $0.373 < \gamma_h < 0.746$.

4. From Eq. (9), the residual circulation on the upper hull is determined as a function of γ_h, that is, $\kappa^+_{hc} = -\kappa^-_{hb} - \kappa^+_{ft} = (0.042 \times R^2/\gamma_h) - 3$, see Fig. 36(b).

5. By using Eq. (35), K_1 is solved as a function of γ_h, see Fig. 36(c).

6. Once K_1 and K_2 are known from the above steps, the remaining coefficients K_f and K_h as functions of γ_h are obtained by least-squares fitting Eqs. (36) and (37) to the force-and-moment data, see Fig. 36(c).

7. From Eqs. (38)-(41), the model coefficients (A, B, C and D) are determined as functions of γ_h, see Fig. 36(c).

To summarise with an example say $\gamma_h = 1/2$, this gives a lower-hull circulation $-\kappa^-_{hb} = A \times R^2/\gamma_h = 0.042 \times 7.3^2/(1/2) = 4.5$. A fin-tip vortex of strength $\kappa^+_{ft} = 3$ leaves on the upper-hull casing a residual circulation $\kappa^+_{hc} = -\kappa^-_{hb} - \kappa^+_{ft} = 4.5 - 3 = 1.5$. Hence, substituting the values $\kappa^-_{hb} = -4.5$, $\kappa^+_{ft} = 3$, $\kappa^+_{hc} = 1.5$, $\gamma_h = 1/2$ and $\gamma_f = 3/4$ into Eqs. (35) and (22) yields $K_1 = 0.540$ and $K_2 = 0.240$. By least-squares fitting the data ($\diamond$, Figs. 34 and 35) in the range $5^\circ \le \psi \le 15^\circ$,

$$C_{F_y} = [0.074\cos(\psi) + 0.0192]\ \sin(\psi), \tag{50}$$
$$C_{M_z} = [0.020\cos(\psi) + 0.0029]\ \sin(\psi), \tag{51}$$

with r.m.s. errors of 9% and 3% respectively, the remaining coefficients $K_f = 0.584$ and $K_h = 0.546$ are solved.

11 Concluding Remarks

A model of the flow around a generic conventional "Joubert" submarine hull form at pure yaw has been constructed from surface-streamer visualisation and flow-topology concepts. The purpose of this work is to gain some understanding of the large-scale (vortical) structures produced by the hull which can affect the motion control, manoeuvring and signature of the submarine.

The flow-topology model (e.g. Fig. 31) shows the presence of a pair of counter-rotating longitudinal vortices on the leeward side of the hull. The inclusion of a fin (or sail) on the upper hull further produces a U-shaped vortex. This U-shaped vortex consists of three segments: (i) a bound vortex which spans the height of the fin, connected to (ii) a vortex leg along the tip of the fin and (iii) a vortex leg along the upper hull. Just above the upper hull, the rotation sense of the vortex leg arising from the fin is opposite to that of the vortex leg arising from the nose, and so these vortex legs act to cancel each other (the resulting structure F_{hc} is shown in Fig. 31).

An analytical treatment of the topology model has provided an initial step towards developing equations which relate the sway-force and yaw-moment coefficients to the hull-form geometry and the circulation of the surrounding flow. The model equations (36) and (37) take into account the fin location and the slenderness ratio of the hull. They can be calibrated by using circulation, force and moment data from experiments and/or computational-fluid-dynamics (CFD) modelling, and therefore can serve to cross-check/validate experimental and CFD data.

Future refinements may take into account other factors such as casing geometry, control surfaces, experimental arrangement of sting or pylon support(s), submarine propulsion and the Reynolds number to obtain general equations for sway force and yaw moment.

12 Acknowledgements

Thanks go to Chetan Kumar and Paul Jacquemin for assisting with the flow-visualisation experiment, to Gregory Seil and Lincoln Erm for refereeing this document, and to Howard Quick for providing the experimental force and moment data for the generic conventional Joubert submarine geometry. The financial support from the SEA1000 project is gratefully acknowledged.

References

1. Joubert, P. N. (2004). Some aspects of submarine design part 1: hydrodynamics. Technical Report 1622, DSTO.

2. Joubert, P. N. (2006). Some aspects of submarine design part 2: shape of a submarine 2026. Technical Report 1920, DSTO.

3. Hunt, J. C. R., Abell, C. J., Peterka, J. A., and Woo, H. (1978). Kinematical studies of the flows around free or surface-mounted obstacles; applying topology to flow visualisation. *Journal of Fluid Mechanics*, 86:179–200.

4. Tobak, M. and Peake, D. J. (1982). Topology of three-dimensional separated flows. *Annual Review of Fluid Mechanics*, 14:61–85.

5. Goett, H. J. and Bullivant W. K. (1938). Tests of N.A.C.A. 0009, 0012, and 0018 airfoils in the full-scale tunnel. Report 647, NACA.

6. Erm, L. P. (2003). Calibration of the flow in the extended test section of the low-speed wind tunnel at DSTO. Technical Report 1384, DSTO.

7. Kumar, C., Manovski, P., and Giacobello, M. (2012). Particle image velocimetry measurements on a generic submarine hull form. In *Proceedings of the 18th Australasian Fluid Mechanics Conference, paper 188*, Launceston, Australia.

8. Anderson, B., Chapuis, M., Erm, L., Fureby, C., Giacobello, M., Henbest, S., Jones, D., Jones, M., Kumar, C., Liefvendahl, M., Manovski, P., Norrison, D., Quick, H., Snowden, A., Valiyff, A., Widjaja, R., and Woodyatt, B. (2012). Experimental and computational investigation of a generic conventional submarine hull form. In *29th Symposium on Naval Hydrodynamics*, Gothenburg, Sweden.

9. Fureby, C., Anderson, B., Clarke, D., Erm, L., Giacobello, M., Henbest, S., Jones, D., Nguyen, M., Johansson, M., Jones, M., Kumar, C., Lee, S.-K., Manovski, P., Norrison, D., Patterson, K., Seil, G., Woodyatt, B., and Zhu, S. (2014). Experimental and numerical study of a generic conventional submarine at 10-degrees yaw. In *30th Symposium on Naval Hydrodynamics*, Hobart, Australia.

10. Ashok, A. and Smits, A. J. (2013). The turbulent wake of a submarine model in pitch and yaw. In *51th AIAA Aerospace Sciences Meeting, paper 2013-1121*, Grapevine, Texas, USA.

11. Simpson, R. L. (2001). Junction flows. *Annual Review of Fluid Mechanics*, 33:415–443.

12. Ölçmen, S. M. and Simpson, R. L. (1995). An experimental study of a three-dimensional pressure-driven turbulent boundary layer. *Journal of Fluid Mechanics*, 290:225–262.

13. Chow, J., Zilliac, G., and Bradshaw, P. (1997). Turbulence measurements in the near field of a wingtip vortex. Technical Memorandum 110418, NASA.

14. Giuni, M. (2013). *Formation and early development of wingtip vortices*. Ph.D. Thesis, School of Engineering. University of Glasgow, United Kingdom.

15. Helmholtz, H. (1867). LXIII. On integrals of the hydrodynamical equations, which express vortex-motion. *Philosophical Magazine Series 4*, 33:226, 485–512.

16. Green, S. I. (1995). *Fluid Vortices*, Kluwer Academic Publishers.

17. Munson, B. R., Young, D. F., and Okiishi, T. H. (2002). *Fundamentals of Fluid Mechanics*, 4th edition, John Wiley & Sons, Inc.

18. Jeans, T. L. (2007). *An estimation method for the normal force distribution on slender axisymmetric bodies with tapered tails*. Ph.D. Thesis, Department of Mechanical Engineering. University of New Brunswick, Canada.

19. Jeans, T. L., Watt, G. D., Gerber, A. G., Holloway, A. G. L., and Baker, C. R. (2009). High-resolution Reynolds-averaged Navier-Stokes flow predictions over axisymmetric bodies with tapered tails. *American Institute of Aeronautics and Astronautics Journal*, 47:19–32.

20. Jeans, T. L., Holloway, A. G. L., Watt, G. D., and Gerber, A. G. (2010). A force estimation method for viscous separated flow over slender axisymmetric bodies with tapered tails. *Journal of Ship Research*, 54:53–67.

21. Lamb, H. (1932). *Hydrodynamics*, 6th edition, Dover Publications.

22. Jones, R. T. (1946). Properties of low-aspect-ratio pointed wings at speeds below and above the speed of sound. Report 835, NACA.

23. Quick, H., Widjaja, R., Anderson, B., Woodyatt, B., Snowden, A. D., and Lam, S. (2012). Phase I experimental testing of a generic submarine model in the DSTO low speed wind tunnel. Technical Note 1101, DSTO.

24. Quick, H. and Woodyatt, B. (2014). Phase II experimental testing of a generic submarine model in the DSTO low speed wind tunnel. Technical Note 1274, DSTO.

25. Johnson, H. S. (1953). Wind-tunnel investigation at low speed of the effect of varying the ratio of body diameter to wing span from 0.1 to 0.8 on the aerodynamic characteristics in pitch of a 45° sweptback-wing-body combination. Research Memorandum L53J09a, NACA.

26. Pitts, W. C., Nielsen, J. N., and Kaattari, G. E. (1953). Lift and center of pressure of wing-body-tail combinations at subsonic, transonic, and supersonic speeds. Report 1307, NACA.

27. Brich, D., Lee, T., Mokhtarian, F., and Kafyeke, F. (2004). Structure and induced drag of a tip vortex. *Journal of Aircraft*, 41:1138–1145.

28. Anderson, E. A. and Lawton, T. A. (2003). Correlation between vortex strength and axial velocity in a trailing vortex. *Journal of Aircraft*, 40:699–704.

29. Seil, G. and Anderson, B. (2013). Computational Fluid Dynamics Manoeuvring Simulation of DSTO Generic Submarine with different Fins. Client Report 2013-0385, DSTO.

DEFENCE SCIENCE AND TECHNOLOGY GROUP DOCUMENT CONTROL DATA	1. DLM/CAVEAT (OF DOCUMENT)

2. TITLE	3. SECURITY CLASSIFICATION (FOR UNCLASSIFIED REPORTS THAT ARE LIMITED RELEASE USE (L) NEXT TO DOCUMENT CLASSIFICATION)
Topology Model of the Flow around a Submarine Hull Form	Document (U) Title (U) Abstract (U)
4. AUTHOR	5. CORPORATE AUTHOR
S.-K. Lee	Defence Science and Technology Group 506 Lorimer St, Fishermans Bend, Victoria 3207, Australia

6a. DST GROUP NUMBER	6b. AR NUMBER	6c. TYPE OF REPORT	7. DOCUMENT DATE
DST-Group–TR–3177	AR-016-453	Technical Report	December, 2015

8. FILE NUMBER	9. TASK NUMBER	10. TASK SPONSOR	11. No. OF PAGES	12. No. OF REFS
–	–	SEA1000	50	29

13. DST Group Publications Repository	14. RELEASE AUTHORITY
`http://dspace.dstg.defence.gov.au/dspace/`	Chief, Maritime Division

15. SECONDARY RELEASE STATEMENT OF THIS DOCUMENT

Approved for Public Release

OVERSEAS ENQUIRIES OUTSIDE STATED LIMITATIONS SHOULD BE REFERRED THROUGH DOCUMENT EXCHANGE, PO BOX 1500, EDINBURGH, SOUTH AUSTRALIA 5111

16. DELIBERATE ANNOUNCEMENT

No Limitations

17. CITATION IN OTHER DOCUMENTS

No Limitations

18. DST GROUP RESEARCH LIBRARY THESAURUS

Submarine; Flow Visualisation; Topology; Circulation; Sway Force; Yaw Moment

19. ABSTRACT

A topology model constructed from surface-streamer visualisation describes the flow around a generic conventional submarine hull form at pure yaw angles of 0°, 10° and 18°. The model is used to develop equations for sway-force and yaw-moment coefficients which relate to the hull-form geometry and the flow circulation around the submarine.